García Martínez, A.; Monsalve-Serrano, J.; Martínez-Boggio, SD.; Golke, D. (2023). Energy assessment of the ageing phenomenon in Li-Ion batteries and its impact on the vehicle range efficiency. Energy Conversion and Management. 276. https://doi.org/10.1016/j.enconman.2022.116530

Energy assessment of the ageing phenomenon in Li-Ion batteries and its impact on the vehicle range efficiency

Antonio García*, Javier Monsalve-Serrano, Santiago Martinez-Boggio, Diego Golke

Energy Conversion and Management
Volume 276, 15 January 2023, 116530
https://doi.org/10.1016/j.enconman.2022.116530

CMT - Motores Térmicos, Universitat Politècnica de València, Camino de Vera s/n, 46022 Valencia, Spain

Corresponding author (*):

Dr. Antonio García Martínez (angarma8@mot.upv.es)

Phone: +34 963876574

Abstract

The 2035 European Union ban on internal combustion engines pushes the transport industry toward alternative propulsion technologies. One of the most potent alternatives to the 250 million passenger automobiles in Europe is the use of electric vehicles with lithium-ion batteries as a special energy storage system. To develop a sustainable, money-saving, and mature technology like today's internal combustion engines, however, issues including battery deterioration, charging times, and safety must be addressed. In this study, Lithium Ferrum Phosphate and Nickel Manganese Cobalt, two distinct cathode chemistries indicative of transport solutions, are compared for cell performance and ageing. It is possible to improve battery design to increase capacity and lower the risk of thermal runaway by using experimental and numerical methods to evaluate and predict the battery ageing effect. The calibrated ageing model may also forecast battery life and its effect on the vehicle's driving range. The findings indicate that the Lithium Ferrum Phosphate cathode chemistry has a lower energy density and ages more quickly than the Nickel Manganese Cobalt, resulting in a shorter driving range. In specifically, a brand-new Nickel Manganese Cobalt battery provides 84 km of additional city driving range and 50 km of highway driving range over a Lithium Ferrum Phosphate battery. The Nickel Manganese Cobalt battery offers 53 km more driving range on the interstate and 91 km more in urban driving at the end of its useful life (20% capacity loss).

Keywords

Battery Modeling; Ageing; Capacity fade; Driving Range

1. Introduction

The best near-term solutions to reduce the CO_2 emissions from the transport sector are electric vehicles (EVs) and hybrid electric vehicles (HEVs) [1]. Both concepts increase the powertrain efficiency using lithium-ion (Li+) batteries as an energy storage system. However, to increase the market penetration and driving range, one of the most urgent requirements is to develop high-energy-density cells, which frequently raises concerns related to reliability and safety. In addition, cell degradation with vehicle usage reduces the vehicle driving range due to the decrease in battery performance as solid interface and lithium plating grow [2]. As an aggravating factor, at higher battery temperatures, several exothermic chemical reactions can occur inside a cell. This may generate heat accumulation, accelerating the chemical reaction between the cell components. In cases where the heat transfer to the surroundings is insufficient, thermal runaway can occur [3].

System simulations are an effective way to obtain results while reducing testing costs and time. Lithium-ion cells are a significant task due to the long period for degradation testing (calendar ageing around years and cycling ageing around months) and the expensive costs of thermal runaway experimental tests due to the destruction of the cells. For performance description of lithium-ion cells under pristine and aged cells, electrochemical models proposed by Newman [4] are demonstrated as an accurate option. Several works use equivalent circuit models (ECM) [5] because they are a faster solution, but have limitations in terms of ageing prediction. Accurately describing the degradation behaviours of lithium-ion batteries is critical for the correct design of the battery pack and the future improved battery management systems in EVs. In general, lithium ion batteries (LIBs) ageing involves capacity loss, impedance rise, and power fade. Battery performance declines over time due to irreversible chemical and physical degradation.

A dominant process is the solid electrolyte interface (SEI) growth. The SEI formation is a complex electrochemical reaction that occurs during the first charge of the cell, and it produces a passivating layer between the positive and negative electrodes when carbon anodes are used. The process is not yet fully understood, and authors have been proposing root causes for the SEI growth. The most accepted theory is related to the co--intercalation of solvent molecules, along with Li+ ions into the graphite structure of the anode or also due to the decomposition of the electrolytes on the graphite surface [6]. The SEI is made of inorganic and organic lithium (Li) salts and has an outer porous layer and a dense inner layer [7]. Its formation is influenced by many factors, such as electrolyte composition and graphite bulk and surface properties. In principle, this is the desired process as it protects the negative electrode, suppressing any further decomposition of the electrolyte and preventing exfoliation of the graphite electrode. However, the SEI can degrade and become unstable under certain battery operating conditions [8]. For instance, these working conditions include high state of charge (SOC), high and low temperatures outside the recommended, over-voltage, under-voltage and over-currents. The main effect of SEI growth over time is the decrease of cyclable Li-ions, reducing the battery capacity.

While most of the cited phenomena occur on the negative electrode, the positive electrode undergoes ageing due to the wear of active material. Nevertheless, SEI growth

is recognized as the leading cause of ageing under normal usage conditions. The mechanisms of ageing can be further divided into three classes: loss of lithium inventory (LLI), loss of active material (LAM) that can occur on both positive and negative electrodes, and degradation of reactions kinetics [9]. As anticipated, ageing occurs during battery use and storage. Calendar ageing refers to the battery degradation during rest conditions (storage). Regarding battery degradation due to usage, Wang et al. [18] estimated the life cycle under different operating temperatures, current rate or C-rate (defined as the capacity of a battery is commonly rated at 1C, meaning that a fully charged battery rated at 1Ah should provide 1A for one hour). and depth of discharge (DoD) for a LiFePO4. The results showed that cycle life has an exponential decay for increasing temperatures. Also, as higher the DoD, the higher is the capacity fade. But, this behaviour decreases if lower C-rates are used.

There are two types of ageing models [10]: 1) Empirical models and 2) Chemical degradation models. The first uses experimental results to build a fitting formula, which should be able to describe battery degradation in different scenarios encompassed [11]. Furthermore, empirical models require little knowledge about electrochemical processes that take place in the cell. However, extensive testing is needed to calibrate the models. Even then, inaccurate predictions can occur if the model is employed for cases that deviate from the parameterization test conditions. The second uses an approach based on electrochemical modeling, which can simulate the interaction between battery cell components.

This work establishes a physics-based battery capacity degradation model coupled with chemical/mechanical degradation mechanisms to address the abovementioned problems. Performance and ageing tests were carried out to calibrate and validate the model of the proposed lithium-ion cells with different ambient temperatures and different C-rates. A complete geometric characterization of the battery in terms of particle size, electrode and separator thickness, electrode capacity, battery internal resistance, heat transfer coefficient, SEI porosity, among others is presented. The data obtained with the model, validated in different ambient conditions and battery demands (constant and dynamic currents), were used as a support to give an insight into thermal issues related to the ageing process and to estimate the vehicle autonomy range considering the battery capacity fade. The novelty of this work is based on the coupling of a Pseudo 2D battery model with vehicle simulations to estimate the driving range as well as to monitor the battery state of health during the driving cycle. The future vehicle battery management systems will incorporate complex models to help extending the battery life. The current and temperature control are critical to minimize the battery degradation. This work contains all the parameters to model a NMC and LFP cylindrical cells typically used in electric vehicles. The experimental tests are also presented in detail to be used or replicate in future works.

2. Methods

Samsung INR18650-20R (NMC) and NX 9073 (LFP) cells were used for this study, with the main characteristics presented in Table 1. The first one has a lithium-Ion Nickel Rechargeable (INR) cathode chemistry with a nomenclature: Nickel-Manganese-Cobalt oxide ($LiNiMnCoO_2$). This type of cell is also referred to as NMC hybrid chemistry, which

has the advantage of increased energy capacity compared to the Lithium Cobalt Oxide (LCO) and Lithium Iron Phosphate ($LiFePO_4$, LFP) chemistries. NMC battery boasts a 2 Ah capacity that provides 169 Wh/kg, while LFP battery has a nominal capacity of 1.8 Ah, resulting in 139 Wh/kg.

NMC and LFP voltages at fully charged condition are 4.2V and 3.65V, respectively, and both have the cut-off voltage (minimum safety voltage) at 2.5 V. Both anodes are composed of graphite, as most of the lithium-ion cells in the market. The selected batteries have low internal resistance and a long life cycle, offering long storage life of three months or more. The standard charge for these batteries is 180 min (100 mA cut-off), and a rapid charge is 50 min at 25°C (100 mA cut-off).

Table 1. Main Lithium-Ion cell properties for the NMC and LFP cathodes.

Parameter	NMC	LFP
Cell format	18650	18650
Cathode Chemistry	$LiNiMnCoO_2$	$LiFePO_4$
Anode Chemistry	Graphite	
Electrolyte Chemistry	Lithium hexafluorophosphate, organic carbonates	
Dimensions [mm]	18.3 x 65.0	18.2 x 65.2
Weight [g]	42.4	41.5
Nominal Voltage [V]	3.6	3.2
Nominal Capacity [Ah]	2.0	1.8
Current Charge Continuous/Peak [A]	2.0/4.0	1.8/-
Current Discharge Continuous/Peak [A]	22.0/30.0A	5.4/10
Total Energy [Wh]	7.2	5.8
Vent Cap holes	3	3
Voltage at 100% SOC [V]	4.2	3.65
Cut-off voltage [V]	2.5	2.5
Temperature use Range [℃]	-20 to 60	-20 to 50

2.1. Experimental setup

The present work was developed with two leading types of equipment simulating several battery operating conditions. Experimental tests with controlled ambient temperature (cycling purpose) were conducted with different battery power demands. A bidirectional current source was coupled with an ARC to achieve these goals.

The bidirectional current source of type Arbin LBT 10V 100A 001E02582, manufactured by Arbin Instruments, was used. This equipment aims to supply current to charge the batteries following a specific protocol and simulate a load on batteries that require different power demands. The equipment has four channels capable of providing a voltage range from 0 to 10V with a control accuracy of ± 4 mV. Also, the Arbin's laboratory battery testing (LBT) can cover a current range from 500 mA to 100A with a control accuracy of ± 0.04% on full-scale, according to the range used. LBT has a programable interface, where the user can choose different protocols and configure controls based on battery type. The LBT can perform tests with constant current, voltage, C-rate (based on current capacity), power, load (constant resistance), current ramp, voltage ramp, constant current and constant voltage (CCCV protocol). In addition, driving cycle simulation can be performed by imposing time versus current or time versus power data. In this work, constant current discharge rates and transient current profiles representative of the driving cycle of an EV are performed. The charging was done following the CCCV protocol for performance tests and constant current up to maximum voltage for ageing tests.

The ambient temperature control for cycling and performance tests was performed by an accelerating rate calorimeter (ARC), model ARC THT EV+, manufactured by Thermal Hazards Technologies. Furthermore, the calorimeter works as a safety chamber for destructive testing due to its robustness and cooling system. Essentially, the calorimeter has electric resistances on the top, side and bottom surfaces, which heat the interior and work as adiabatic boundaries. In this way, there are two modes by which the ARC can control the ambient temperature: Iso-thermal and heat-wait-seek. In both methods, the ambient temperature can be controlled with a precision of ±0.2%. The iso-thermal mode maintained a fixed ambient temperature and was used to perform ageing and performance tests of pristine and aged batteries. The ARC is equipped with N-type thermocouples with 0.001°C resolution and an accuracy of 0.7% to control the ambient temperature.

Type K thermocouples measured battery surface temperature throughout the performance and ageing tests. These temperature data were recorded using an Agilent 34901A Datalogger. Battery voltage and current were measured and acquired by the Arbin system. The acquisition rate of all equipment was set to 10 Hz and triggered to start recording simultaneously. Figure 1a and Figure 1b show the CMT facilities used for this work. A scheme of the equipment and measurement systems is presented in Figure 1c.

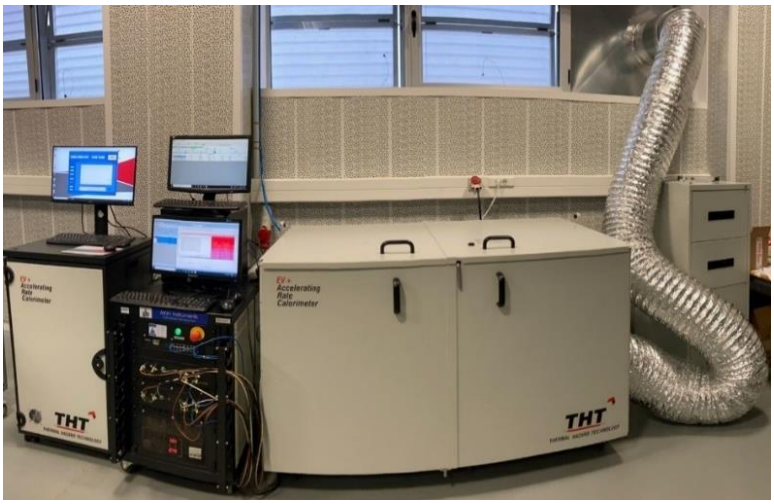

(a)

(b)

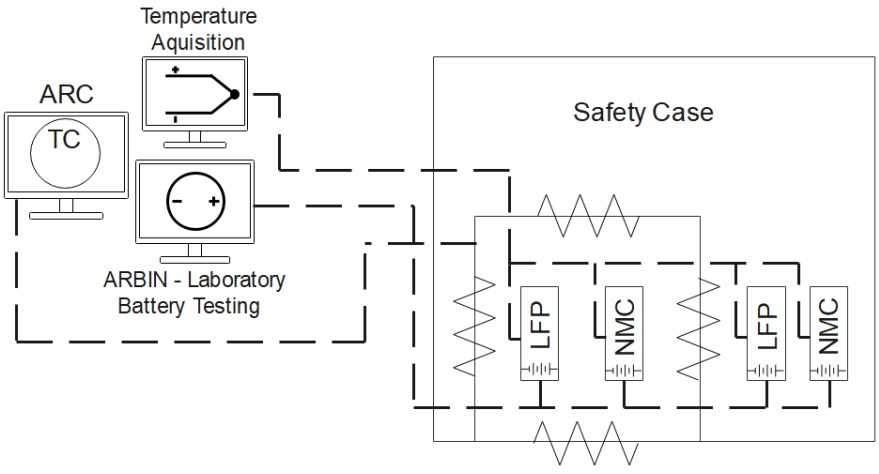

(c)

Figure 1. Experimental Set up with the ARC EV+ and current source in CMT-UPV battery lab (a), the set up measurement system (b) and the scheme of the batteries connection for the testing (c).

2.2. Test procedure

The constant current constant voltage (CCCV protocol) was used to charge the batteries before performance tests. The charging procedure begins with a constant current of 1 C-rate up to the maximum voltage, according to the battery manufacturer. During the constant voltage charging phase, the current progressively decreased to a value of 5% of 1 C-rate. After, the batteries were left to rest for 30 minutes (zero current) at room temperature. Then, the discharge process occurred with constant current according to the C-rate demanded. The performance tests were carried out at $\frac{1}{6}$, $\frac{1}{2}$, 1 and 3 C-rate.

In addition to the tests mentioned above with constant C-rate, performance under transient load was also tested. The current profile was imposed in the power supply representative of driving conditions. A SUV electric vehicle is studied with a battery of around 70 kWh to have an acceptable vehicle range. A virtual model is performed and the battery package is built with the same cells tested in this work. Therefore, the cell current profile of the virtual vehicle was taken and experimentally imposed on the cell. As a hypothesis, the cell package has a voltage of 600V and the same number of parallel cells for both NMC and LFP. The 70 kWh of total energy storage is achieved with 60 parallel cells. Meanwhile, the series cells are 167 for NMC and 187 for LFP. The total energy of the package is 72 kWh for the NMC and 65 kWh for the LFP. This approach's advantage is that both types of cells have the same current profile. Therefore, for the experimental campaign, one current profile is imposed for both cathode chemistries. The cell weight in the proposed NMC battery package is 424 kg (10020 cells x 0.424 kg), while for the LFP is 465 kg (11220 cells x 0.415 kg). In addition, the battery enclosure, cooling system, controller and cabling were added to the final vehicle weight. Following the work of Löbberding et al. [12], 40% of the specific energy density, considering only the battery cells, is reduced when considering the whole package. Thus, the NMC battery pack will have a total weight of 593 kg against 651 kg from the LFP pack. These values are used for the complete vehicle weight calculation.

In summarizing, Figure 2 depicts a scheme of the voltage and current behaviour as a function of time when the CCCV charge protocol, constant C-rate, and discharge transient profile is applied in the battery. These profiles are used for the experimental campaign to determine the performance under different ambient temperatures.

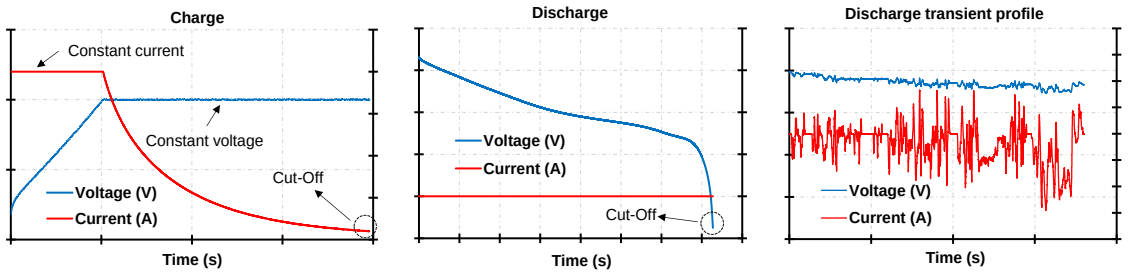

Figure 2. Charge, Discharge, and transient profiles protocols used for the battery testing.

After the performance test, the degradation tests were performed. The charge process during the cycling tests (ageing tests) was different from that used in the performance due to the long time required for battery ageing. Therefore, the constant current of 1 C-rate up to maximum voltage was used. The battery rested for 30 minutes in sequence, and a discharge process occurred. For the cycling test, the discharge rate was 2 C-rate to have more severe conditions and save testing time. The ambient

temperature remained constant due to the ARC controller with a variation of less than 0.2%. In such a manner, charge and discharge cycles were carried out with a rest period of 30 minutes between processes. A schematic of the ageing procedure is detailed in Figure 3. The target was to achieve 250 cycles (charge-rest-discharge-rest). This protocol implies 30 days of testing without stopping. The temperature, voltage and current were recorded with a step time of 10 seconds.

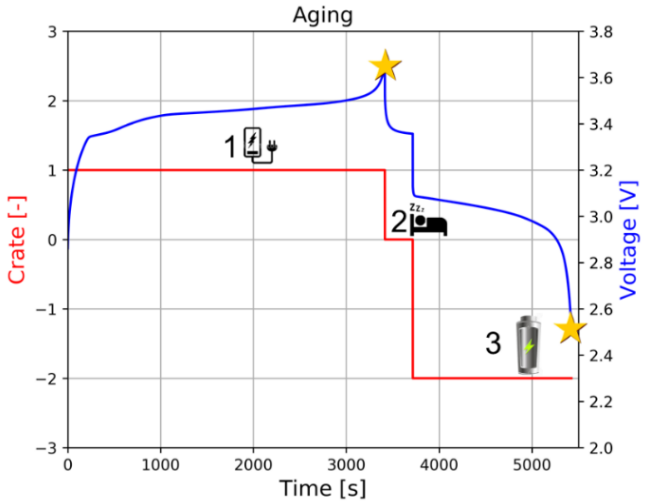

Figure 3. Ageing test protocol with charging, rest and discharge. The values are representative of a LFP cell.

2.3. Modelling framework

This study is developed considering the coupling of different simulation approaches, creating a complete framework for the battery evaluation in terms of cell, module (arrange of cells), and complete package (arrange of modules). This section aims to define the object of study and the relevant information for each modelling approach, such as the equations, validations and coupling strategy.

2.3.1. Lithium-Ion Battery model

A battery model was created with the GT-AutoLion software (Gamma Technologies® v2022) to characterize the battery properties and operation. The model was calibrated and validated with experimental results of performance and ageing. The mentioned software allows scaling the behaviour of one cell to model a battery module and package. It is possible to link the battery to another subsystem like a complete vehicle model or an electric machine.

The cell model corresponds to a pseudo-2D physicochemical model initially developed by Newman et al. [4] for predicting battery performance by estimating the reaction rate at which lithium ions and electrons are transferred from cathode to anode, considering resistance growth and temperature changes during the battery operation. The model is accompanied by a database of material properties that covers most commercially available chemistries in the market for cathode, anode, electrolyte, or separator. Still, it is also possible to modify these properties to accommodate the user needs.

On top of this electrochemical model, a series of degradation mechanisms are included to account for battery ageing as solid electrolyte interface growth, lithium plating and others. Also, other mechanisms like a mechano-electrochemical model for strain prediction from active material swelling or a double-layer capacitance model are available for more detailed and specific studies. It is evident that the software's capabilities cover most user needs, but this can be overwhelming when attempting to calibrate the model and fit the experimental measurements if not simplified. For this reason, the current approach focuses on the basic electrochemical model under non-extreme operating conditions. The first step neglects ageing effects to understand better how this calibration procedure should be applied in a pristine cell. Later in this work, the ageing parameters are included and calibrated with experimental results.

The electrodes are conceptualized as solid solution particles on the microscopic scale for which species intercalation is modelled based on a surface of exchange and a concentration difference. A longitudinal scale to account for species transport in the macroscopic scale in the electrode is taken. The lithium goes from one electrode to another through the separator, creating the potential difference and defining the current. A general sketch of the conceptualized pseudo-two-dimensional model can be found in Figure 4, showing the longitudinal disposition of the anode and cathode solid phases submerged in the electrolyte. Each component is modelled as a series of particles that adsorb and deliver lithium ions and electrons.

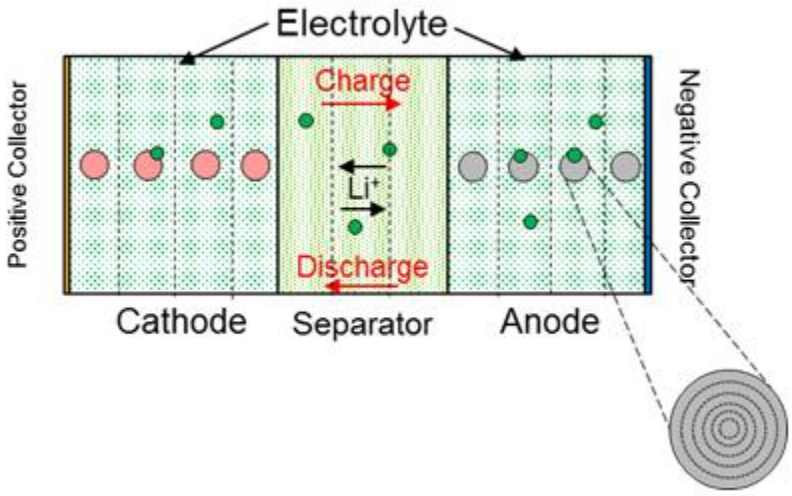

Figure 4. Conceptual sketch of the pseudo-two-dimensional electrochemical model

The essence of the electrochemical model is defined through a set of ordinary differential equations (ODEs). Notably, mass balance and species conservation have two governing equations, one in the particle's radial direction and one for through-plane macroscopic transport. Charge conservation adds another two ODEs for solid phase and electrolyte, respectively, both in the macro scale.

The Butler-Volmer equation that defines lithium intercalation reaction rates is then utilized to give closure to this ODEs system. Because physicochemical properties of the materials are highly dependent on the working temperature of the cell, the temperature evolution requires an additional governing equation for thermal balance. The cell is taken as a lumped mass with different heat sources (electrochemical

reactions, internal resistance, and entropic heat generation) and heat transfer boundaries (convective heat transfer to the ambient).

Species conservation in the electrolyte and active materials

As a general notion, during the redox reactions that take place during the operation of a lithium-ion battery cell, few species appear and disappear and are then transported from anode to cathode through the electrolyte [13,14]. Lithium stored in the active material is separated into lithium ions that travel through the electrolyte and the separator and electrons that create an electric current that travels through the external circuit. Therefore, lithium ions can be considered to only appear on the electrolyte while moving between electrodes. The longitudinal transport of lithium ions is governed by Equation 1, regarding the porous medium and potential difference [15].

$$\frac{\partial}{\partial_x}[\varepsilon c_e] = \frac{\partial}{\partial_x}\left(D_e^{eff}\frac{\partial c_e}{\partial x}\right) + \frac{1-t_+^0}{F} j^{Li} \qquad \text{Eq. 1}$$

where ε is the porosity, c_e is the molar concentration of lithium ions in the electrolyte, D_e^{eff} denotes the electrolyte effective diffusion coefficient, F is the Faraday's constant, t_+^0 is the transference number, and j^{Li} is the reaction current of lithium.

It is worth mentioning that whenever a diffusion coefficient, ionic conductivity, or other transfer parameters are referred to as effective, they are accounting for porosity effects through the Bruggeman relation [16], in which a transport property (A) has an effective value scaled with the porosity of the medium (ε) and the Bruggeman tortuosity exponent (p) as defined by Equation 2. The values of these exponents have been studied by other authors, and a widely accepted hypothesis assumes a value of $p = 1.5$ for mass, thermal, electric, and ionic conductivities [17,18].

$$A^{eff} = A\varepsilon^p \qquad \text{Eq. 2}$$

Once the lithium ions reach the solid electrodes, a reaction to turn them into lithium and an intercalation process take place at the microscale. Based on Fick's law of mass diffusion and the Ohm's law for electrical potential distributions, the concentration of lithium in the radial direction of the particles in the active materials c_s can be described by Equation 3 [19].

$$\frac{\partial c_s}{\partial_x} = \frac{1}{r^2}\frac{\partial}{\partial_x}\left(D_s r^2 \frac{\partial c_s}{\partial r}\right) \qquad \text{Eq. 3}$$

being r the radius of the particle and D_s the diffusion coefficient of lithium in the solid phase.

Charge conservation in the solid and electrolyte phases

The involvement of potential differences in the transport of species and the current generation also demands considering charge transport in the equations. Also, different formulations must be applied given the different nature of charge transport through the liquid electrolyte and through the solid phases of active material. In the

Doyle-Fuller-Newman (DFN) model, the derivation of the main equations is based on the hypothesis of electroneutrality, which defines that a volume element within the porous electrode will be, in essence, electrically neutral. This is because it requires a large electric force to create a separation of charge over an appreciable distance. In the case of solid phases, the electrons are transmitted mainly by electric conductivity. Then, the reaction current can be defined by the formula in Equation 4:

$$0 = \frac{\partial}{\partial_x}\left(\sigma_s^{eff}\frac{\partial \phi_s}{\partial x}\right) - j^{Li} - a_{dl}C\frac{\partial(\phi_s - \phi_e)}{\partial x} \qquad Eq.4$$

where σ_s^{eff} is the effective solid-phase conductivity, ϕ_s is the solid phase potential and j^{Li} is the reaction current of lithium. The additional term refers to double-layer capacitance, considering ϕ_e as the liquid phase potential, a_{dl} as the specific interfacial area and C as the particular capacitance.

In the case of the electrolyte, current flow occurs mainly through ionic and diffusional conductivity. The presence of electrons and lithium ions in the electrolyte can lead to the formation of metallic lithium, considered one of the main degradation mechanisms in the literature. However, such a source of lithium losses is not considered. With this assumption, the electric potential through the electrolyte is expressed as in Equation 5.

$$0 = \frac{\partial}{\partial_x}\left(k^{eff}\frac{\partial \phi_e}{\partial x}\right) + \frac{\partial}{\partial_x}\left(k_D^{eff}\frac{\partial lnc_e}{\partial x}\right) + j^{Li} + a_{dl}C\frac{\partial(\phi_s - \phi_e)}{\partial x} \qquad \text{Eq. 5}$$

where k^{eff} is the electrolyte effective ionic conductivity, and c_e the Li^+ concentration in the electrolyte. The parameter k_D^{eff} is the ionic diffusional conductivity that can be obtained by Equation 6.

$$k_D^{eff} = \frac{2RTk^{eff}}{F}(t_+^0 - 1)\left(1 + \frac{dlnf_{\pm}}{dlnc_e}\right) \qquad \text{Eq. 6}$$

with R the gas constant, T temperature, F Faraday's constant, t_+^0 transference number and $f_{\pm}$ the molar activity coefficient in the electrolyte [20].

To relate all four main ODEs described for species and charge conservation, the Butler-Volmer equation represented in Equation 7 defines how the electrical current through an electrode depends on the voltage difference between the electrode and the bulk electrolyte. The equation is derived considering the charge neutrality principle of an electrode-electrolyte interface. It governs the net charge production rate by summing the forward and backward rate of current production [21]. In this equation, a_s is the volume specific reaction surface area, i_0 the exchange current density, α the charge transfer coefficient, R_u the universal gas constant and R_{SEI} the resistive film layer.

$$j^{IC} = a_s i_0\left[e^{\frac{\alpha_a F}{R_u T}\left(\eta - \frac{R_{SEI}}{a_s}j^{Li}\right)} - e^{\frac{\alpha_c F}{R_u T}\left(\eta - \frac{R_{SEI}}{a_s}j^{Li}\right)}\right] \qquad \text{Eq. 7}$$

The overpotential, η, can be defined as the difference between the solid (ϕ_s) and liquid (ϕ_e) phases potentials, minus the open-circuit potential of the solid (U):

$$\eta = \phi_s - \phi_e - U \quad \text{Eq. 8}$$

One of the main concerns of this equation is the symmetry between the charge transfer coefficient for anode (α_a) and cathode (α_c). Some studies show that under extreme temperature conditions, non-symmetric behaviour can be observed [22]. Nonetheless, the most common hypothesis is that both parameters take the value of 0.5 [21,23]. Since no extreme conditions are included in this study, this last hypothesis will be maintained for simplicity.

Theoretical capacity and stoichiometry for a battery cell.

During the battery operation, not all the Li content within the active material can be cycled. In this sense, the theoretical capacity $C_{s,max}$ may not be the best parameter to represent the working capacity of the battery cell. Conventionally, the maximum usable capacity of a cell is defined by its first discharge capacity. In addition, other parameters, such as the ratio between the mass-specific first charge capacity (q_{fcc}^{cat}) and mass-specific first discharge capacity (q_{fdc}^{cat}) divided by their mass-specific theoretical capacity (q_{th}^{cat}) can be used to express how the cell deviates from its maximum capacity, as shown in Equation 9 and Equation 10.

$$\gamma_{fcc}^{cat} = \frac{q_{fcc}^{cat}}{q_{th}^{cat}} \quad \text{Eq. 9}$$

$$\gamma_{fdc}^{cat} = \frac{q_{fdc}^{cat}}{q_{th}^{cat}} \quad \text{Eq. 10}$$

where γ is the ratio of first discharge and first charge capacity. Therefore, the cathode stoichiometry can be defined as presented in Equation 11.

$$Stoichimetry = \frac{C_s}{C_{s,max}} \quad \text{Eq. 11}$$

Thermal balance of the cell

For the cell temperature evolution that will affect the transfer properties of the materials, an additional differential equation is included governing the energy balance [24]. A zero-dimensional thermal mass in which heat transfer to the ambient and heat generation from the electrochemical model is accounted can be written as Equation 12. Heat transfer to the ambient is reduced to convective heat transfer to the ambient temperature since no cooling or external thermal management system is included in the study.

$$\rho c_p \frac{dT}{dt} = \dot{q}_{gen} + \frac{hA_c(T - T_{amb})}{V_c} \quad \text{Eq. 12}$$

The heat sources during the cell operation include several mechanisms, which comprehend the heat generated during the redox reactions ($\dot{q}_{rxn}$), the reversible heat generated during intercalation and de-intercalation processes coming from lithium

movements ($\dot{q}_{rev}$), the ohmic heat due to electronic and ionic flows within the cell ($\dot{q}_{ohm}$), and the heat generated due to contact resistance at the current collectors ($\dot{q}_c$). Irreversible entropic heat generation can be accounted for within the term $\left(\frac{\partial U}{\partial T}\right)$ that denotes the changes of the open circuit potential with temperature. Equation 13 to Equation 15 show the definition of each of these terms following Bernardi's model [25,26].

$$\dot{q}_{gen} = \dot{q}_{rxn} + \dot{q}_{rev} + \dot{q}_{ohm} + \dot{q}_c \quad \text{Eq. 13}$$

$$\dot{q}_{rxn} = \frac{1}{L}\int_0^L j^{Li}\eta \, dx \quad \text{Eq. 14}$$

$$\dot{q}_{rev} = \frac{1}{L}\int_0^L j^{Li}\left(T\frac{\partial U}{\partial T}\right) dx \quad \text{Eq. 15}$$

$$\dot{q}_{ohm} = \frac{1}{L}\int_0^L \left[\sigma^{eff}\left(\frac{\partial \phi_s}{\partial x}\right)^2 + \kappa^{eff}\left(\frac{\partial \phi_e}{\partial x}\right)^2 + \kappa_D^{eff}\left(\frac{\partial lnc_e}{\partial x}\right)\left(\frac{\partial \phi_e}{\partial x}\right)\right] dx \quad \text{Eq. 16}$$

$$\dot{q}_c = \frac{R_c}{A_s V_c} I^2 \quad \text{Eq. 17}$$

All these parameters need to be fit to model the cell behaviour. A set of manipulability parameters are optimized against experimental data obtained in the laboratory by a genetic algorithm (GA). The constructive characteristics and electrochemical design attributes subject to fitting are listed below:

- Cathode, anode, and separator thicknesses [µm].
- First charge capacity of anode and cathode [mAh/g].
- First discharge capacity of anode and cathode [mAh/g].
- Particle size of the anode and cathode active material [µm].
- Specific heat capacity of the cell [J/(kgK)].
- Convective heat transfer coefficient [W/(m²K)].
- Contact Resistance [Ωm²].
- Anode and Cathode capacity [Ah].

In addition, constructive elements, like the thickness of each material layer that composes the cell, are added. The total charge capacity of the cell is considered through a series of parameters that define the lithium inventory available and the capacity of each electrode to allocate the lithium. Finally, thermal effects have been modelled through the convective heat transfer, heat capacity, and other variables intimately related to heat generation, like contact resistance. All the previous variables interact complexly to define the overall cell behaviour. The genetic algorithm iteratively modifies

the value of the 14 input variables within prescribed bounds to minimize the objective function.

The objective function of the GA optimization procedure is the minimization of the voltage and temperature error between the simulated curves and the real response when a specific current profile is applied to the cell. The temperature profile is introduced in the optimization process but with a lower weight in the objective function [27]. The relative discrepancies in the temperature profile have lower importance than in the voltage response. It has been included just to check that the thermal parameters selected by the algorithm are coherent. The objective function is expressed mathematically in Equation 18.

$$E_{ov} = \frac{1}{n} \cdot \sum_{k=1}^{n} \left(w_V \cdot \frac{E_V^k}{f_V} + w_T \cdot \frac{E_T^k}{f_T} \right) \quad \text{Eq. 18}$$

$$E_V^k = \sqrt{\frac{\int_{t_{start}^k}^{t_{end}^k} \left(V_{sim}^k(t) - V_{exp}^k(t) \right)^2 dt}{\left(t_{end}^k - t_{start}^k \right)}} \quad \text{Eq. 19}$$

$$E_T^k = \sqrt{\frac{\int_{t_{start}^k}^{t_{end}^k} \left(T_{sim}^k(t) - T_{exp}^k(t) \right)^2 dt}{\left(t_{end}^k - t_{start}^k \right)}} \quad \text{Eq. 20}$$

where f_V and f_T are the normalization terms of the voltage and temperature error, respectively. Besides, n is the total number of experimental profiles (signals) used in the calibration process, and w_V and w_T are the weight factors of the voltage and temperature profiles. The index k refers to each voltage and temperature profile participating in the calibration procedure.

Three experimental tests were used to calibrate the parameters, including a constant discharge test and a driving cycle. Figure 5 shows the current profiles for the NMC Samsung 20R of 2 Ah. The constant discharge current of 1/6 C-rate (0.33 A) and 3 C-rate (6 A) were used. Also, the driving cycle represents the current profile when an SUV with a battery package of 70 kWh performs the WLTC European homologation cycle. Due to the large capacity of the battery package, the current of one cell is in a low C-rate (-2A < I < 2A). Positive and negative values mean discharge and charge currents, respectively. Similar results were used for the LFP NX9073 with 1.8 Ah.

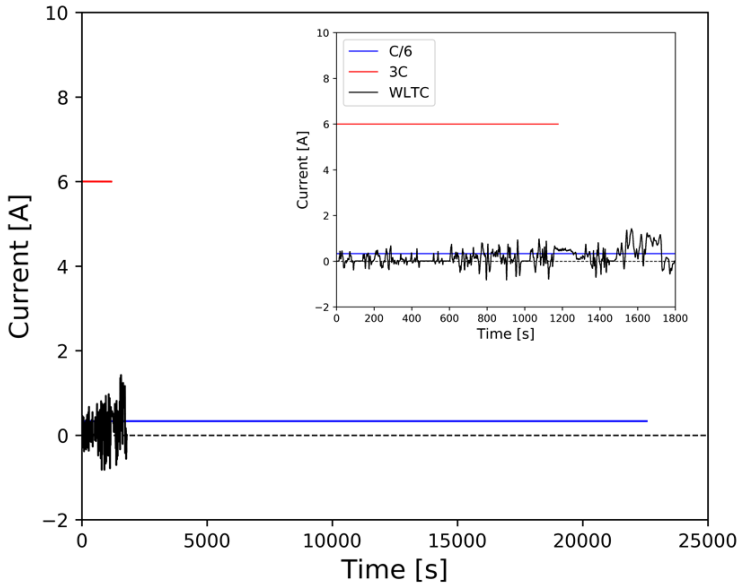

Figure 5. Current intensity profile for the validation of the electrochemical model in constant discharge (a) and driving cycle (b). The values are representative for NMC Samsung 20R.

2.3.2. Ageing model description

In addition to the described equations, other equations are needed to explain ageing effects, such as the growth of the SEI. The SEI forms due to the reaction between the electrolytic components, which break down due to the reducing potential near the anode, and the lithium ions and electrons on the anode side. In this way, the growth in the electrolyte interface is related to the side reaction current density (j_{SEI}) as:

$$j_{SEI} = -a_s i_{0,SEI} exp\left(-\frac{a_{c,SEI} F}{RT}\left(\phi_s - \phi_e - U_{SEI} - \frac{j^{Li}}{a_s} R_{SEI}\right)\right) \quad \text{Eq. 21}$$

being U_{SEI} the equilibrium potential for the chemical reaction, ϕ_s the solid phase potential, ϕ_e the liquid phase potential, j^{Li} the total current density, a_s the volume specific reaction surface area, R_{SEI} the resistance of the SEI layer, and $i_{0,SEI}$ is the exchange current of the side reaction that has a direct dependence on the concentration of electrolyte components at the reaction surface (c_{EC}^s). The exchange current ($i_{0,SEI}$) can be calculated as:

$$i_{0,SEI} = SEI_{rate}\, c_{EC}^s\, F \quad \text{Eq. 22}$$

with F the Faraday constant. The current density can be converted to a scalar number by dividing the superficial area of the reaction. The current is the main parameter responsible for SEI growth, decreasing its values as the SEI thickness increases. Therefore, the current is calculated with Equation 23.

$$i_{SEI} = \frac{j_{SEI}}{a_s} \qquad \text{Eq. 23}$$

The kinetic rate coefficient for the electrochemical reaction responsible for SEI layer growth is calculated with Equation 24, which is based on an Arrhenius equation that takes into account the temperature effects.

$$SEI_{rate} = SEI_{rate,ref} exp^{\left[\frac{E_{a,SEI}}{R}\left(\frac{1}{T_{ref}}-\frac{1}{T}\right)\right]} \qquad \text{Eq. 21}$$

Where $SEI_{rate,ref}$ represents the pre-exponential factor, $E_{a,SEI}$ is the activation energy and R is the universal gas constant.

The SEI layer is formed due to the reaction between electrolyte components and the lithium ions and electrons in the anode, separating the electrolytic substance from the electrode after formation. Thus, the continued growth of SEI layer depends on the diffusion rate of the electrolyte components through the SEI layer, which is described Bruggeman relationship as

$$D_{EC}^{eff} = D_{EC}(\varepsilon_{SEI})^n \qquad \text{Eq. 22}$$

Being ε_{SEI} the solid electrolyte interface porosity, n the Bruggeman exponent, D_{EC} the electrolyte diffusion coefficient. The mass balance for the electrolyte substance diffusion through SEI layer is given by

$$\frac{\partial c_{EC}}{\partial t} = D_{EC}^{eff}\frac{\partial^2 c_{EC}}{\partial r^2} \qquad \text{Eq. 26}$$

The thickness variation of the SEI is a function directly proportional to the current and molecular weight of the solid electrolyte interface and inversely proportional to the density of the SEI and the Faraday constant, evidenced in Equation 27.

$$\frac{d\delta_{SEI}}{dt} = -\frac{i_{SEI}}{2F}\frac{M_{SEI}}{\rho_{SEI}} \qquad \text{Eq. 27}$$

The porosity of the anode decrease as the SEI layer increases the thickness, leading to poor Li-ion transport, increasing the cell resistance. Thus, the porosity change is calculated considering the SEI growth in the following way

$$\frac{d\varepsilon}{dt} = -a_s\frac{d(\delta_{SEI})}{dt} \qquad \text{Eq. 28}$$

By solving the mentioned equations, the resistance and effective conductivity of the electrolyte through the porous SEI layer can be calculated as, respectively.

$$R_{SEI} = \frac{\delta_{SEI}}{K_{SEI}^{eff}} \quad \text{Eq. 29}$$

$$K_{SEI}^{eff} = K_{SEI}(\varepsilon_{SEI})^{n} \quad \text{Eq. 30}$$

The density (ρ_{SEI}) and porosity (ε) of the SEI are taken as parameters for calibrating the ageing mechanism by a genetic algorithm. In addition, the activation energy ($E_{a,SEI}$) is included in the optimization parameters. The experimental results at ambient temperature of 50 ^{o}C and 250 cycles are taken to calibrate the NMC and LFP cells. Due to the low number of cycles, low charge current applied and non-use of low ambient temperature, lithium plating was avoided in this study.

3. Results and discussion

This section, divided into four subsections, contains the results and discussion about the proposed methodology. The performance tests are shown first because this subsection contains all the experimental results to characterize the lithium-ion cells. The second subsection shows the pseudo 2D electrochemical model calibration and validation under pristine conditions. Later, the ageing tests are showed in the third subsection. Lastly, the fourth subsection shows the ageing electrochemical model parameters calibration and validation as well as the driving distance prediction for an electric sport utility vehicle.

3.1. Performance test

Figure 6a and Figure 6b depict the battery voltage as a function of capacity for different C-rates and ambient temperatures. For both cathode chemistries, the lower C-rate and higher ambient temperature resulted in a greater capacity delivered and higher power for the same battery capacity. According to the material safety data sheet provided by the battery manufacturers, the electrolyte substance has as its main ingredients lithium hexafluorophosphate and organic carbonates [28]. Due to the electrolyte's physical-chemical properties, the temperature may have three primary effects on the electrolyte that can change battery performance. Higher temperatures can increase the salt substance dissociation, increasing ion current and delivering higher capacity. Counterbalancing this fact, the higher temperature reduces the dielectric constant of the solvent, which favours the probability of ion associations. However, the greater battery temperature can decrease the electrolyte viscosity, reducing resistance to ion movement during the migration process [29,30]. For these reasons, the net result of higher ambient temperature would be higher capacity delivered due to improved electrolyte conductivity.

Lower C-rates resulted in higher capacity delivered compared to the same ambient temperature. Lower C-rate means that the internal battery reactions occur slowly, improving Li-ion transport efficiency and intercalation/de-intercalation process due to the longer time available, resulting in higher capacity delivered. Furthermore,

comparing the NMC and LFP, the latter has a more voltage plateau curve, which results in a more constant power output (calculated from voltage times current). On the other hand, the NMC has a decreased power output while discharging, which can be not favourable for automotive applications.

Figure 6c and Figure 6d show the battery performance to execute a driving cycle. The cycling carried out with the NMC battery progressively shifted down the voltage curve. Nevertheless, the voltage behaviour looks to be similar throughout the driving cycle. It can be related to the fact that the NMC battery decreased the voltage constantly during a discharge process, as depicted in Figure 6a. On the other hand, the LFP battery has a constant voltage during the discharge process, resulting in a similar performance during subsequent driving cycles as depicted in Figure 6b. Figure 6e and Figure 6f present the effect of temperature on voltage during the driving cycles carried out. No significant difference can be pointed out compared with the battery performance at 20°C.

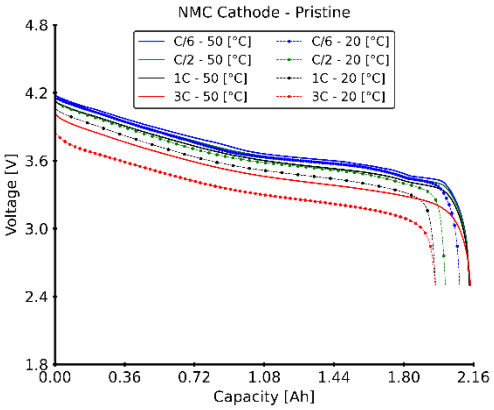

(a)

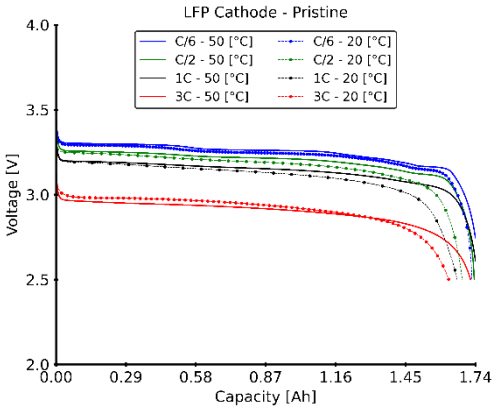

(b)

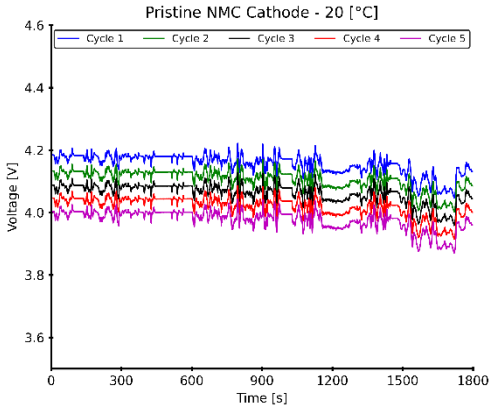

(c)

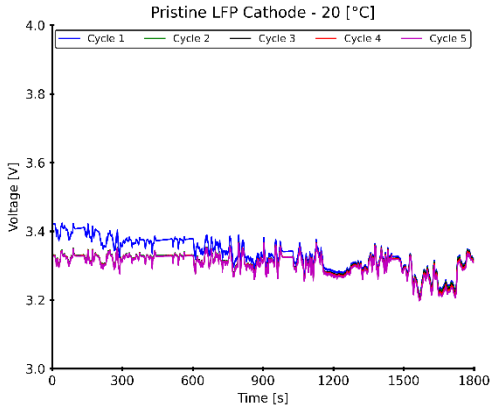

(d)

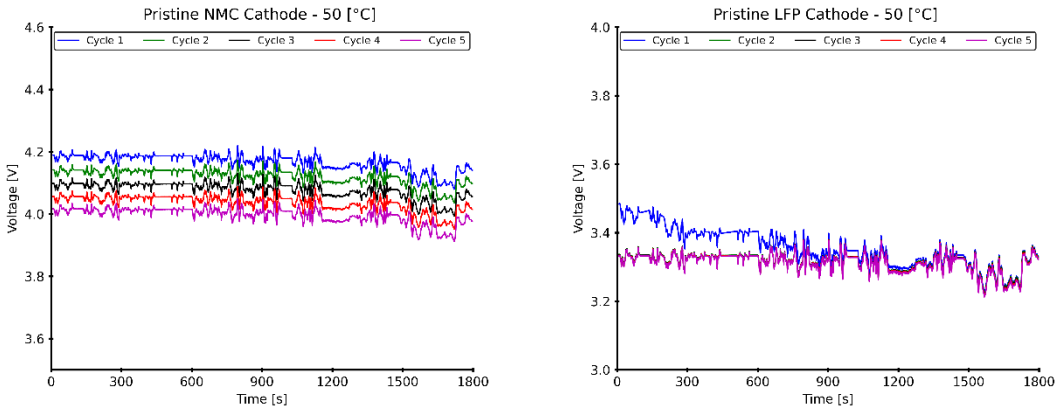

(e) (f)

Figure 6. Constant discharge current and driving cycle performance for two different ambient temperatures for NMC and LFP cells.

Figure 7a and Figure 7b depict the battery temperature as a function of capacity delivered for two different ambient temperatures and different C-rates. Higher C-rates resulted in a higher battery temperature during the discharge process. The higher C-rates increase the battery temperature as an effect of higher local current density and overpotential, increasing the heat generation [31]. However, the higher temperature decreases the battery's internal resistance, which may increase the capacity delivered. This would explain the better performance of batteries working in a higher ambient temperature. However, there is a trade-off effect related to the greater C-rate and same ambient temperature. Despite higher C-rates resulted in higher battery temperature, the discharge capacity is lower when compared with lower C-rates. One reason can be the more prominent drop in dynamic voltage rate, reaching the cut-off voltage before the Li-ion leave the anion, resulting in less discharge capacity [32,33].

In addition, Figure 7c, Figure 7d, Figure 7e and Figure 7f show battery temperature during driving cycles for 20°C and 50°C of ambient temperature. Both cathode chemistries had similar temperature profiles along the driving cycles, with differences not exceeding 2°C.

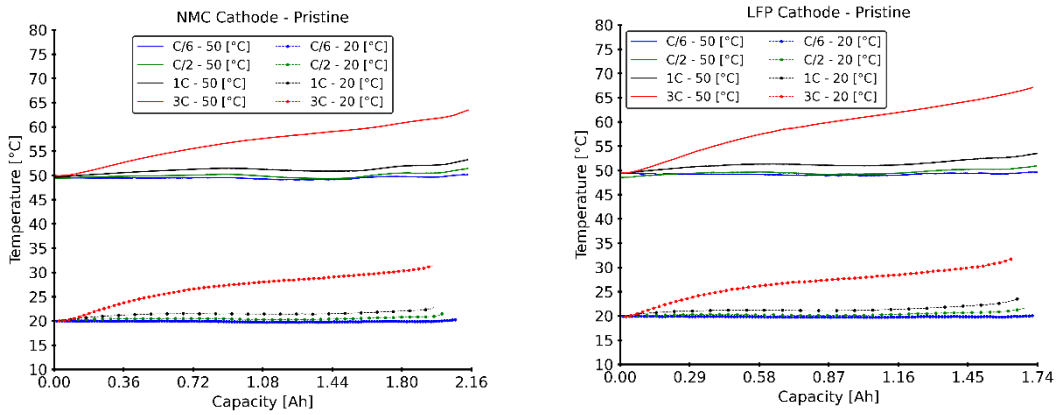

(a) (b)

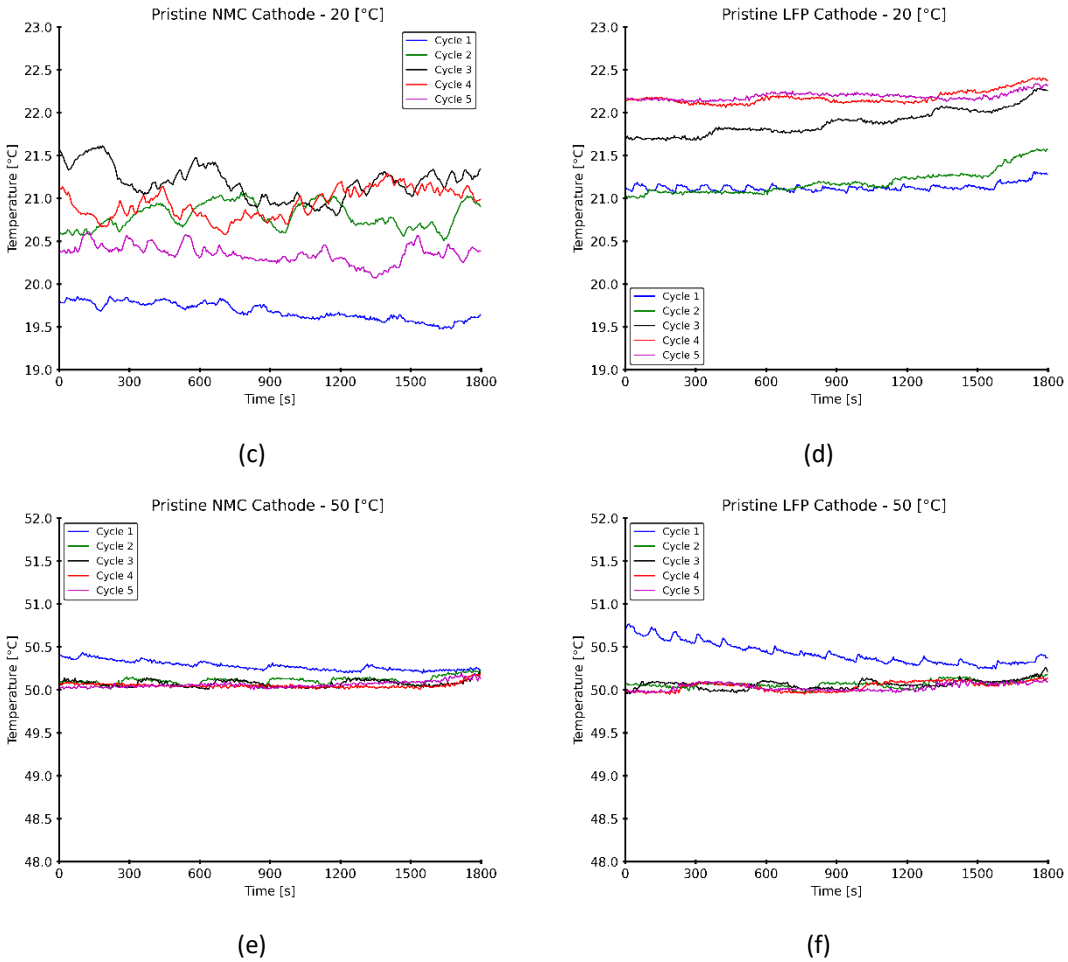

Figure 7. Battery temperature as a function of discharge with different C-rates and along the driving cycles for NMC (left) and LFP (right) cells during ageing testing under ambient temperature of 20°C (top) and 50°C (bottom).

3.2. Electrochemical Model Calibration and Validation

After 1500 simulated cases for each current profile, the genetic algorithm arrives at the best combination of parameters that best adapt for the three cases (C-rate 1/6, 3C and WLTC at 20°C). Figure 8 shows the voltage and Figure 9 temperature profiles for the three mentioned cases. The error for the three cases was, on average, below 2% in voltage and 4% in temperature. Focusing on the voltage profile, the low current (1/6 C-rate) shows an error below 1% and the high current (3 C-rate) below 0.5%. The driving cycle shows even better behaviour (error below 0.4%) because it moves in a narrow range of the cell's total capacity.

The optimum values of the optimization are shown in Table 2. The main difference between the cells is in the cathode side, with higher particle size for the NMC than the LFP. The separator thickness also changes twice for the LFP than the NMC. Moreover, the higher cathode and anode capacity for the NMC makes the overall capacity and energy density greater than the LFP.

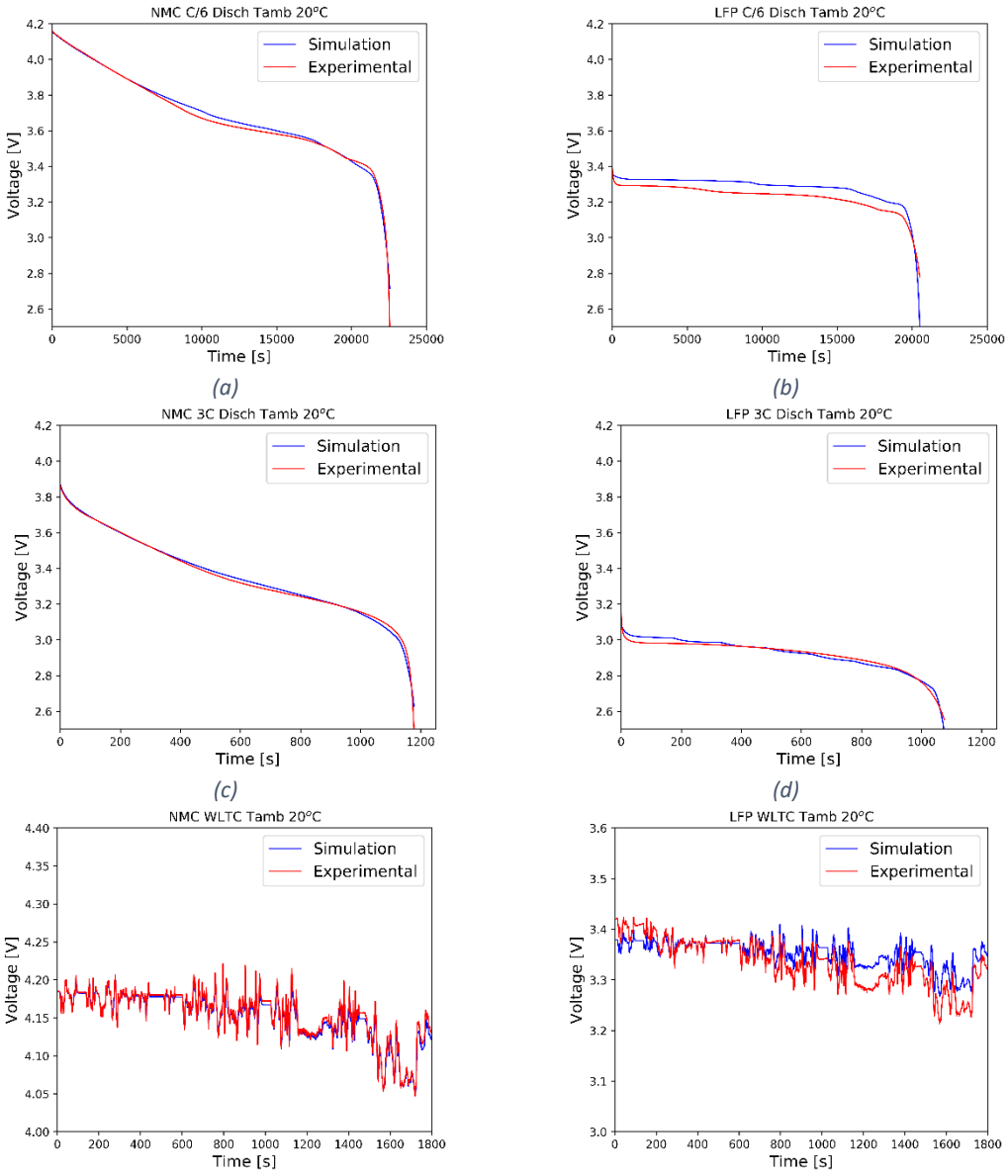

Figure 8. Cell calibration: absolute values of voltage for NMC (left) and LFP (right) for constant current discharge (top) and conduction cycle (bottom).

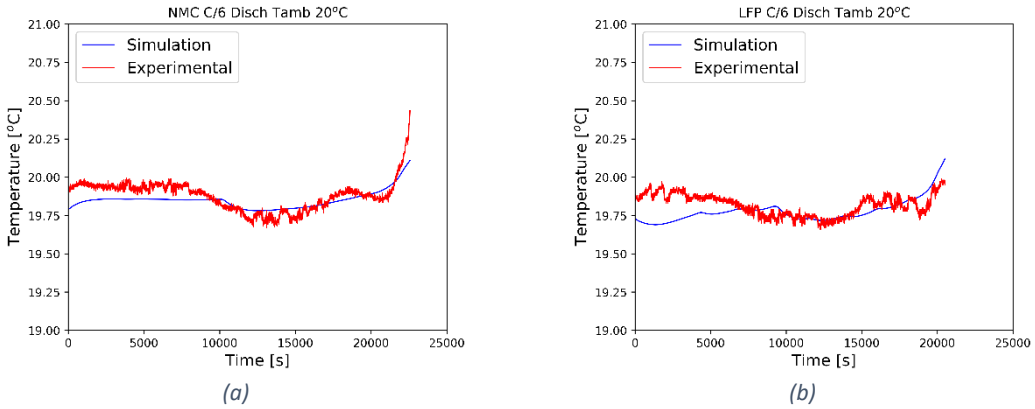

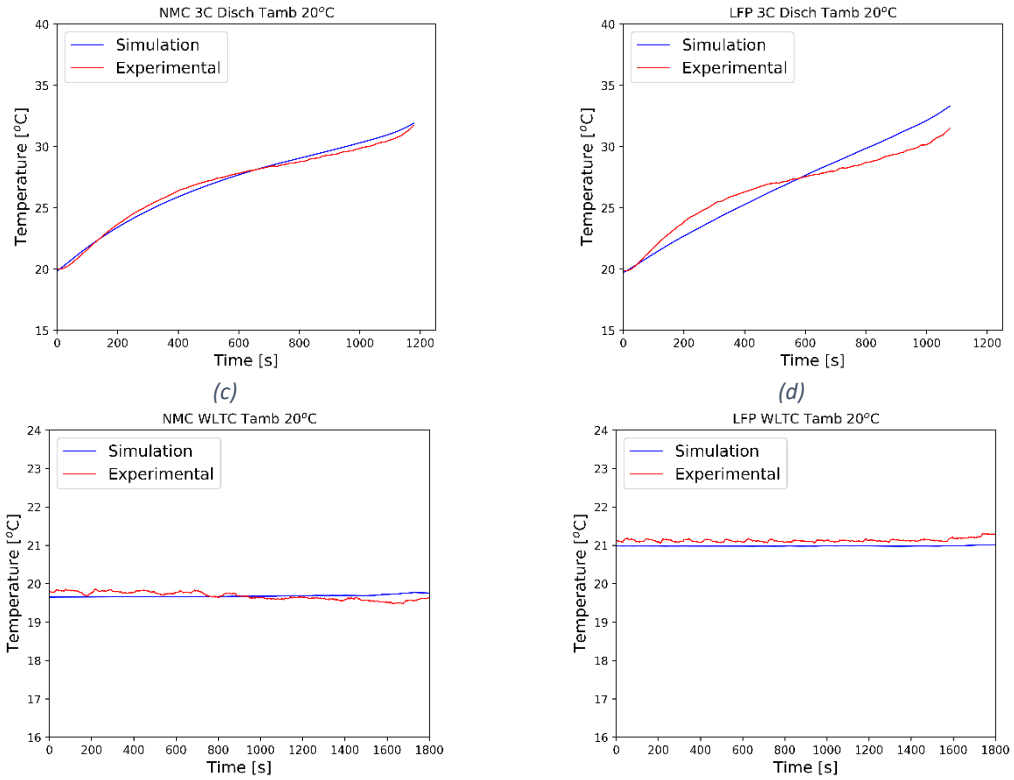

Figure 9. Cell calibration: absolute values of temperature for NMC (left) and LFP (right) for constant current discharge (top) and conduction cycle (bottom).

Table 2. Optimized parameters for NMC Samsung 20R and LFP NX9073 in GT-Autolion.

Parameter	Unit	Range Optimizer	Optimum value NMC	Optimum value LFP
Particle Size Anode	Micron	5 - 30	12.53	10.53
Particle Size Cathode	Micron	0.05 - 30	5.43	0.007
Thickness Anode	Micron	25 - 150	89.12	65.81
Thickness Cathode	Micron	25 - 150	92.14	99.48
Thickness Separator	Micron	5 - 40	26.69	43.14
Cathode Capacity	Ah	2.0 - 6.0	2.47	2.05
Anode Capacity	Ah	2.0 - 6.0	2.76	2.07
Contact Resistance	$mOhm.m^2$	0.1 – 1.0	0.86	1.0
FCC Cathode	mAh/g	150 - 220	193.34	171.76
FDC Cathode	mAh/g	140-210	174.19	166.10
FCC Anode	mAh/g	320-430	403.91	379.37
FDC Anode	mAh/g	300-400	362.86	334.09
HTC	W/m^2K	3 - 40	37.40	26.05
CP	J/kgK	800-1500	1266.61	1255.00

The calibration validation is shown in Figure 10 for NMC and LFP cells. A constant current with 1 C-rate at 20°C and 3 C-rate at 50°C were used. The third curve shows the transient profile at 50°C. The three cases show good agreement with the experimental

curve with an error of around 2% in voltage. The most significant deviation is seen at low SOC due to the sudden voltage loss of the cell. Therefore, for numerical purposes, the SOC variation needs to be maintained between 100% and 20% of SOC.

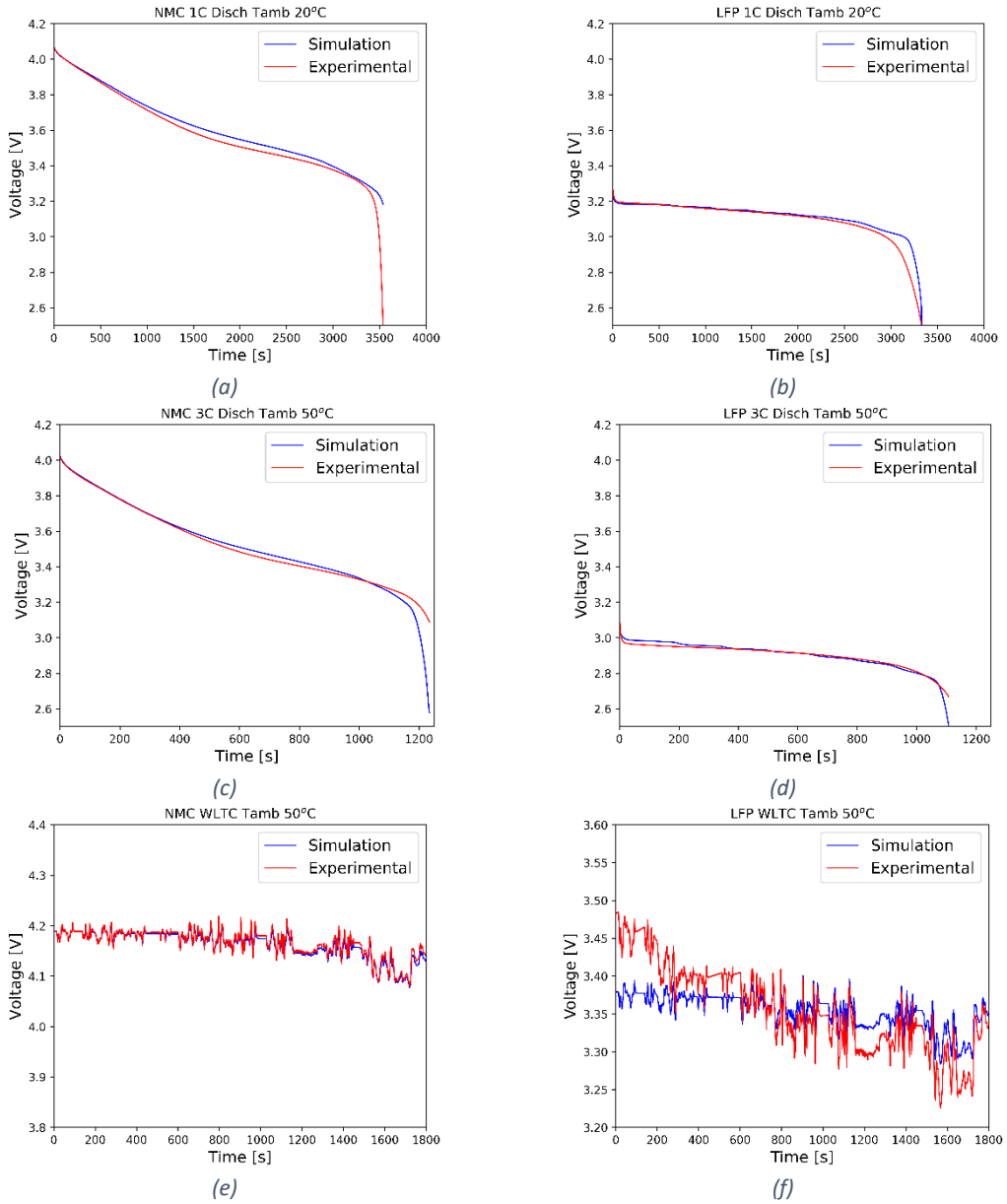

Figure 10. Cell validation: absolute values of voltage (left) and surface temperature (right) for constant current discharge (top) and conduction cycle (bottom).

3.3. Ageing Test

Experimental ageing tests were performed in the NMC and LFP cathode chemistry cells. Figure 11 shows the experimental results regarding voltage for the ageing process of up to 250 cycles submitted in two ambient temperatures. The charge and discharge protocol used were different from that used in the performance tests. In this case, the battery was charged with 1 C-rate up to maximum voltage, resting for 15 min and, in sequence, discharging with 2 C-rates. For the NMC battery at 20°C, Figure 11a, the maximum voltage showed a drop in relation to the NMC battery at 50°C, Figure 11c. One reason may be the charging protocol that does not maintain constant battery voltage

while the current progressively decreases to a minimum value (protocol CCCV). Then, during the rest period, the voltage dropped, resulting in a poor performance delivered during the ageing tests.

According to Figure 11a, Figure 11b, Figure 11c and Figure 11d, the capacity fade was higher at higher ambient temperature for both cathode chemistries. Different mechanisms can cause performance deterioration during battery cycling. At ambient temperature (20°C), the capacity fade is mainly attributed to the solid electrolyte interface growth [34]. However, when the battery is cycled at a higher temperature, such as 50°C, different mechanisms result in a complex system of capacity fade. The loss of lithium inventory is attributed mainly to SEI growth, SEI decomposition and electrolyte decomposition [35]. In addition, other mechanisms, for instance, related to the cathode electrolyte interface, can have a significant effect on the capacity fade, as reported by Wang et al. [36]. For these reasons, higher ambient temperatures result in a higher loss of capacity.

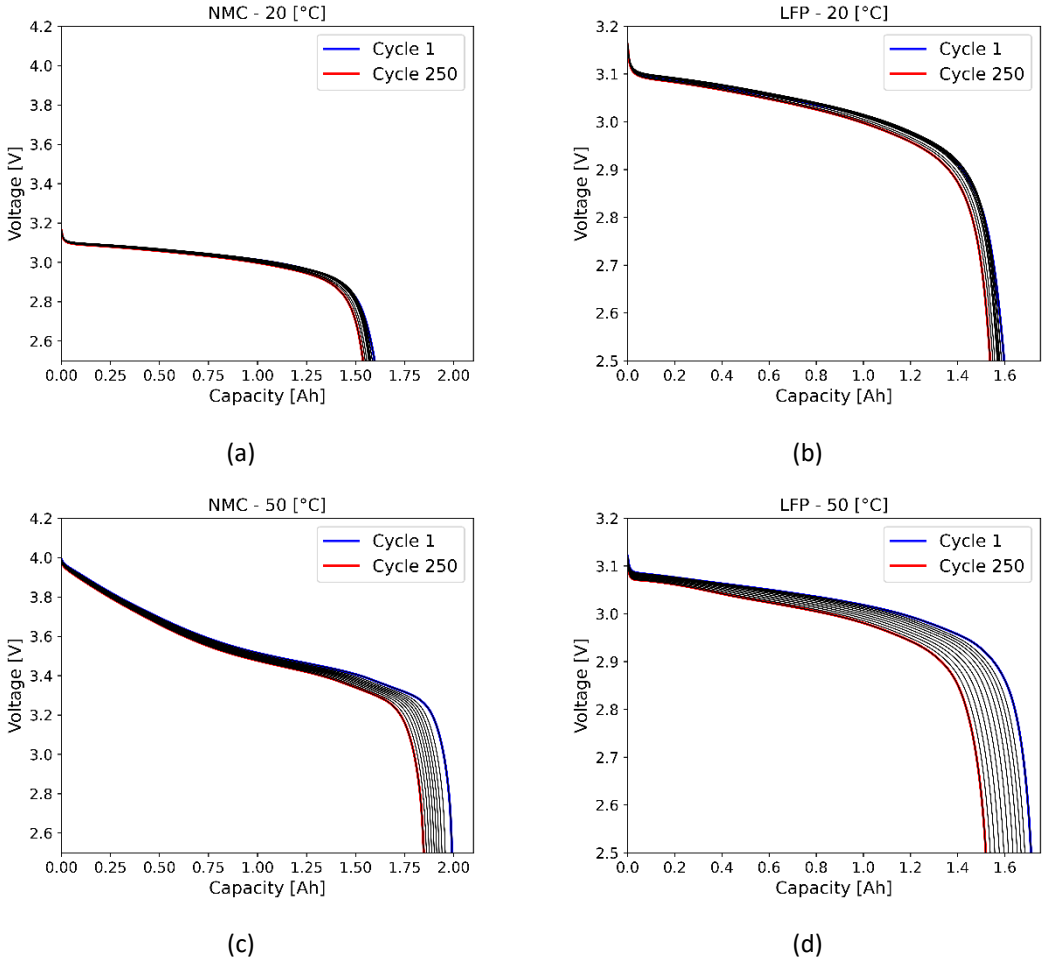

Figure 11. Voltage discharge curve for NMC (left) and LFP (right) cells during ageing testing under ambient temperature of 20°C (top) and 50°C (bottom). Each curve represents a variation of 20 cycles, starting with cycle one (blue line) and finishing with 250 cycles (red line).

Figure 12 depicts the battery temperature over three discharge cycles of the ageing process for NMC and LFP cathode chemistry at two different ambient temperatures. For the ambient temperature at 20°C, the battery temperature difference between the first and last cycle was small, depicting that the ageing process did not

affect the battery temperature in this case. Nevertheless, at 50°C of ambient temperature, the battery temperature difference, green line in Figure 12c and Figure 12d, was higher. The main difference is observed in both batteries' last part of the discharge curve (after 50% of discharge capacity). The degradation due to the ageing process would increase the Joule effect, increasing the battery temperature. In addition, the higher ambient temperature decreases the convection heat transfer between the battery and the environment, resulting in a higher temperature reached by the battery compared to the ambient temperature of 20°C.

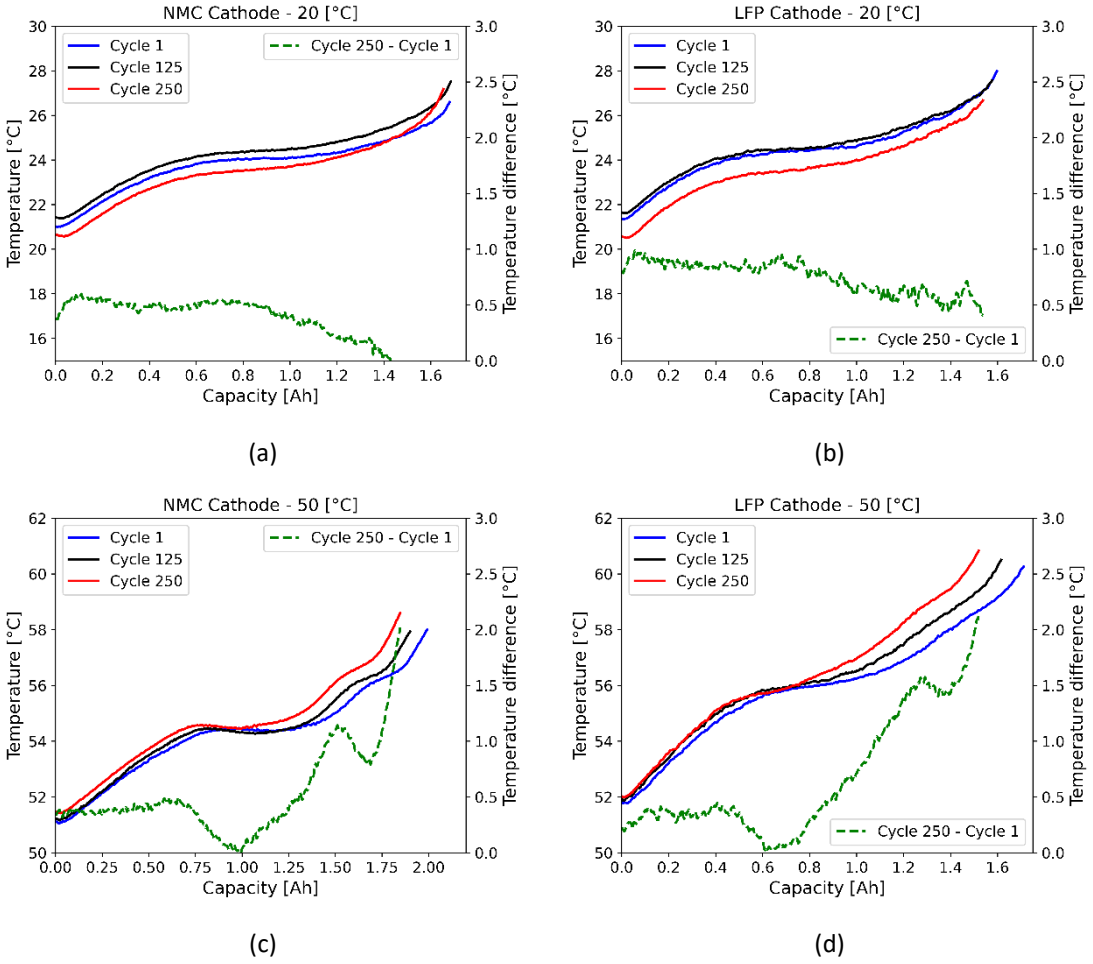

Figure 12. The temperature during discharge curve for NMC (left) and LFP cells (right) in the ageing testing under ambient temperature of 20°C (top) and 50°C (bottom). Cycle one in blue line, cycle 125 in black line and 250 cycles in red line. The difference between 250 cycles and 1 cycle is presented in green dashed line.

Figure 13 summarises the capacity fade as a function of the number of cycles for NMC and LFP at both ambient temperatures. The higher degradation of batteries submitted in a higher temperature ambient is clear. The LFP battery showed a higher reduction in capacity than NMC. The normalized capacity, Figure 13b, was less than 90% of the original performance for LFP battery when it reached 250 cycles. Meanwhile, the NMC battery achieved about 92.5% of the original performance at the end of the ageing process. Decreasing the ambient temperature to 20°C, reduces the capacity fade drastically. However, the degradation process still was higher for the LFP battery.

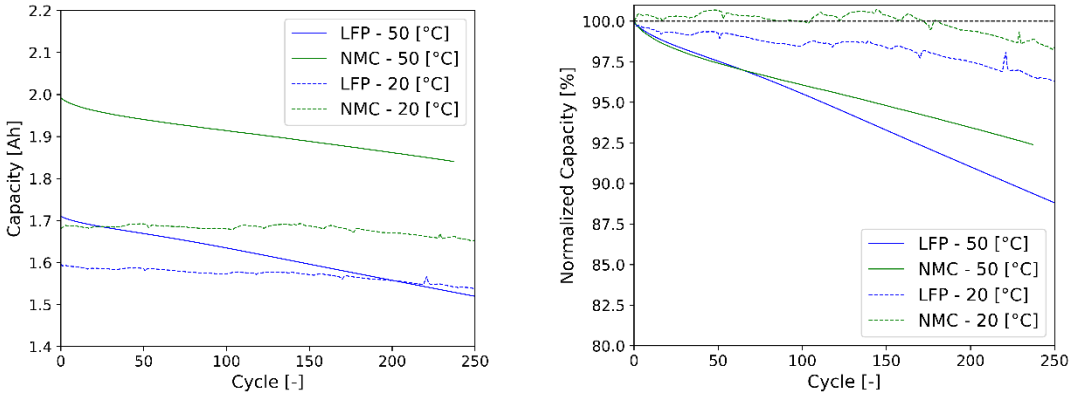

(a) (b)

Figure 13. Cell absolute capacity (a), normalized capacity (b) along the 250 cycles.

Figure 14 presents the capacity delivered of the pristine (Figure 14a) and aged (Figure 14b) batteries (NMC and LFP) as a function of C-rates for two ambient temperatures (20°C and 50°C). NMC and LFP pristine batteries reached the maximum delivery capacity at a higher ambient temperature. In addition, lower C-rates resulted in a higher capacity delivery in general. However, aged batteries showed greater capacity fade when subjected to 50°C ambient temperature, with the NMC battery capacity being similar to at 20°C and the LFP battery capacity being lower than at 20°C.

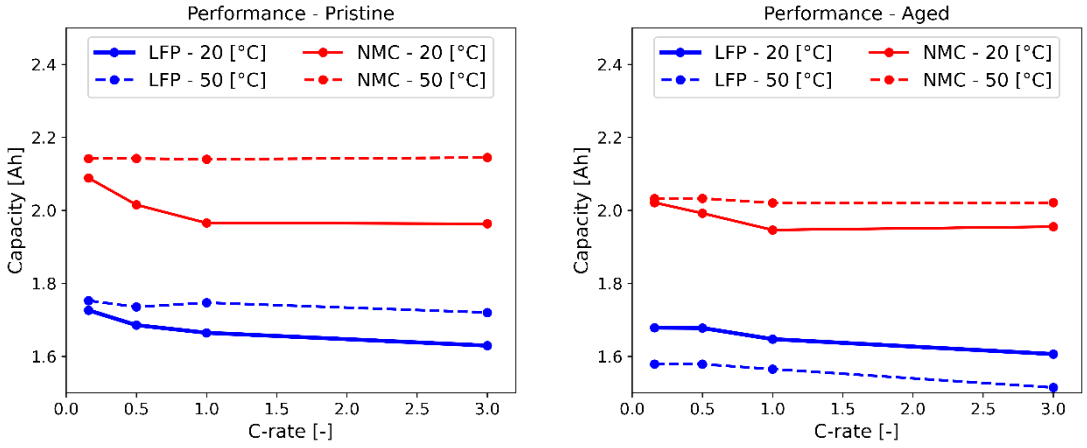

(a) (b)

Figure 14. Capacity of the cell measured by CCCV protocol and discharge with different C-rate for pristine (a) and aged cells (b).

After the capacity test, the driving cycles were performed in the aged cells (250 cycles aged). The same current demand for the pristine cell was applied here (Figure 6). For the brevity of the manuscript, only the global results are shown. The end capacity (Figure 15a) is calculated with the discharge current. It is possible to see the lower capacity of the LFP compared with the NMC. In particular, the LFP aged at 50 °C where the capacity is strongly reduced. Figure 15b shows the estimated vehicle range with all the cases tested. The NMC lead to a similar driving range of around 400 km for all the cases. On the other hand, the capacity reduction makes the LFP goes from 350 km to 305 km.

Figure 16 shows the cell temperature variation for the case at 50ºC ambient temperature. It is possible to see a higher cell surface temperature for the aged cells with around 0.4ºC during all the driving cycles. This is due to the higher internal resistance of the aged cells concerning the pristine ones.

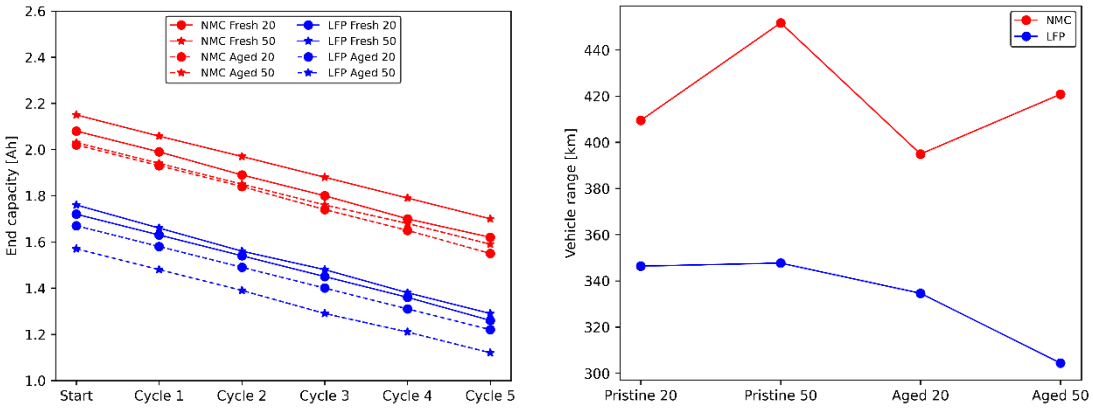

(a) (b)

Figure 15. End capacity after several WLTC cycles (a) and the vehicle range (b) with pristine and 250 cycles cells.

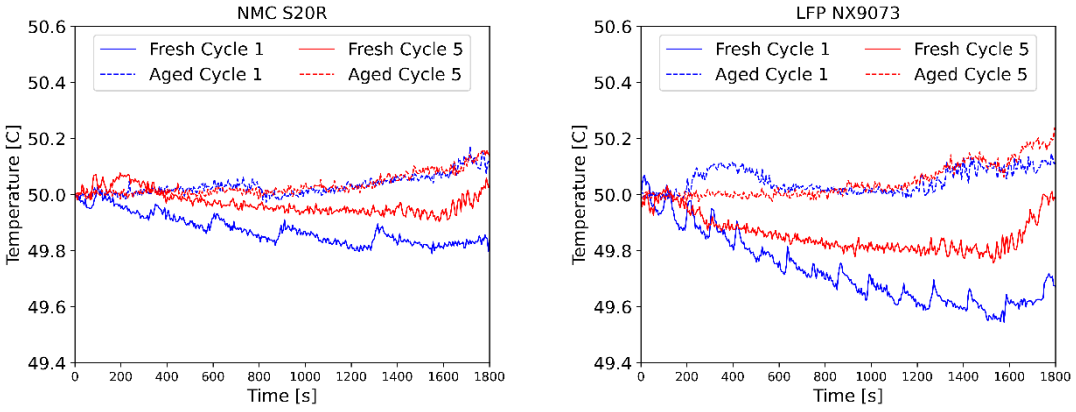

(a) (b)

Figure 16. Cell surface temperature for NMC (a) and LFP (b) during WLTC with pristine and aged cells and ambient temperature of 50ºC.

3.4. Ageing electrochemical model parameters calibration and validation

For the calibration of the aged cell model, GT-Autolion was used with a control model for cell cycling in the same way as used experimentally. Parameters such as remaining capacity, voltage and SOC were obtained. The model is shown in Figure 17. Only the degradation was activated in the anode due to the higher degradation than the cathode. This reduces the optimization process while maintaining the essential degradation mechanism. The mechanism for degradation shown in the methodology section needs to be optimized in terms of SEI density (rho) and SEI porosity. In addition, the mechanism for the SEI reaction rate is optimized by the activation energy (E_a).

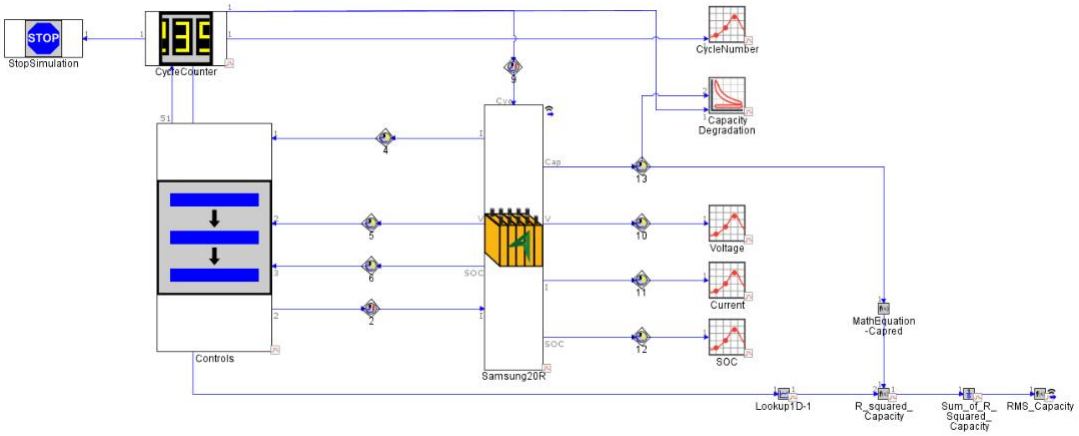

Figure 17. Scheme of the numerical model for the calibration of the aged cell.

The experimental results at 50ºC were used for the calibration since they show a vital degradation with 250 cycles. A genetic algorithm was implemented to optimize three parameters: separator density, separator porosity and activation energy of the separator growth mechanism. The three parameters were adjusted, making the RMS between the experimental curve and the numerical results at cycle number 250 with 1 C-rate of charging and 2 C-rate of discharging. The objective function (RMS of the difference between real and simulated capacity) is shown in Figure 18 for the 140 simulated cases. The high computational cost of this optimization is worth noting since each case represents 250 charge and discharge cycles. However, after the model is calibrated, the advantages come from the possibility to predict the end-of-life, or any other condition during a driving cycle, without further expensive experimental tests. In addition, the path towards the battery end-of-life can be achieved with the model in different conditions such as temperature and power demands. Other methods involving fitting data through interpolation and extrapolation require a considerable number of experimental tests, and sometimes, the model is unreliable in predicting other battery working conditions. The optimizer found the best combination of values after 80 cases. The NMC was easier to optimize with a lower difference with the experimental curve.

The parameter with the most significant influence is the SEI porosity, with a 70% impact, as shown in Figure 19. The optimal value is around 0.1 for both cathode chemistries. The activation energy showed more influence on the LFP than the NMC. However, the SEI density is the second more influential parameter for the ageing mechanism. The final values of the optimization process can be found in Table 3.

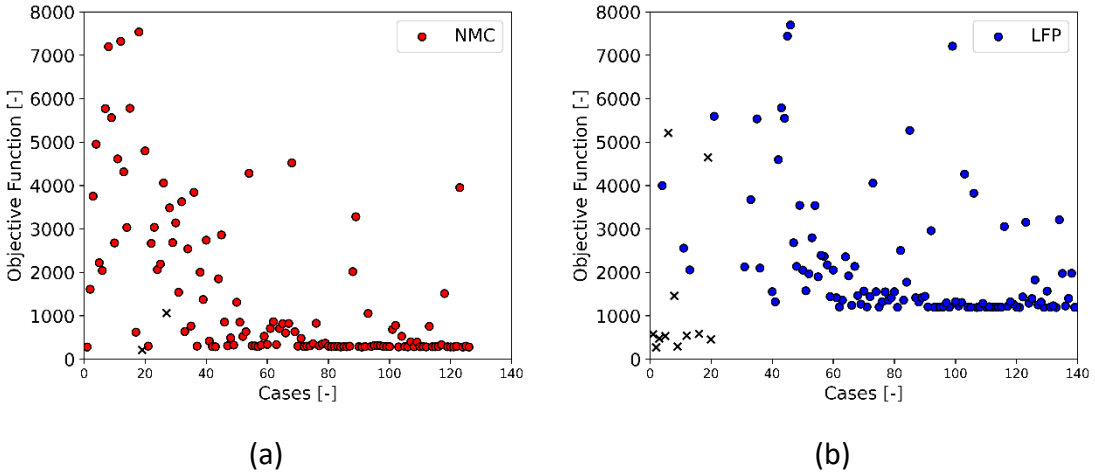

Figure 18. Objective function according to simulated cases for aged cell calibration for NMC (a) and LFP (b).

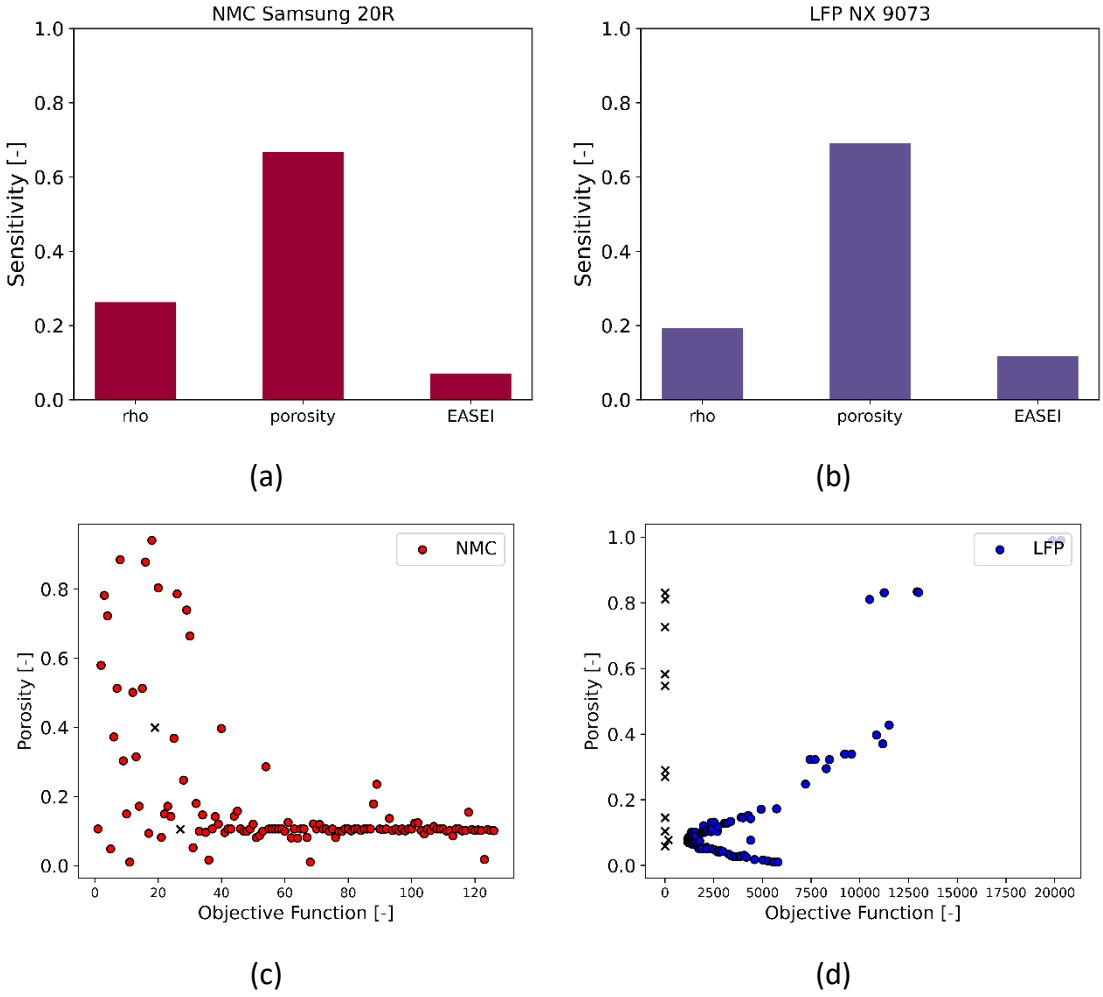

Figure 19. Sensitivity of the optimization parameters for NMC (a) and LFP (b) as well as the value of the most significant parameter that in both cases is the porosity of the cathode fron NMC (c) and LFP (d) according to simulated cases for the aged cell calibration.

Table 3. Optimized ageing parameters for NMC Samsung 20R and LFP NX9073 in GT-Autolion.

Parameter	Unit	Range Optimizer	Optimum value NMC	Optimum value LFP

Rho (ρ_{SEI})	g/cm^3	0.2 – 5.0	3.57	2.08
Porosity (ε)	-	0.001 – 0.99	0.111	0.077
Activation Energy ($E_{a,SEI}$)	J/mol	10 - 10000	35.7	5439.8

The experimental and simulated curve for 250 cycles at 50°C is shown in Figure 20. The difference is less than 1% during all the cycles. The final degradation at 250 cycles for the NMC is -7.3% for the numerical model and 8.0% for the experimental case. For the case of the LFP, the degradation is -11.1% for the simulation and -11.2% for the experimental. Despite the final value is closer for the LFP, the NMC have closer values during the previous cycles. This can also be seen in Figure 18 by the optimizing function. For both cases, the numerical model shows good agreement (<1%) with the experimental results.

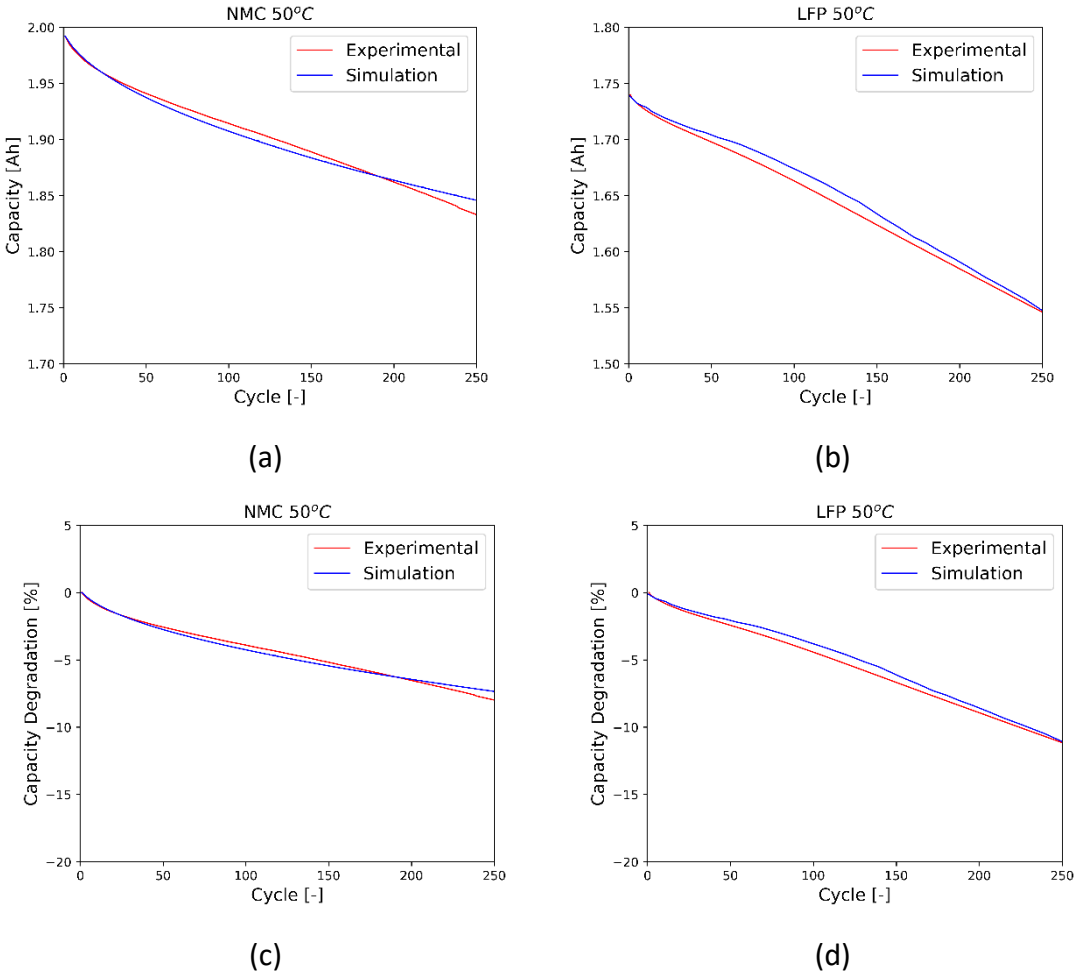

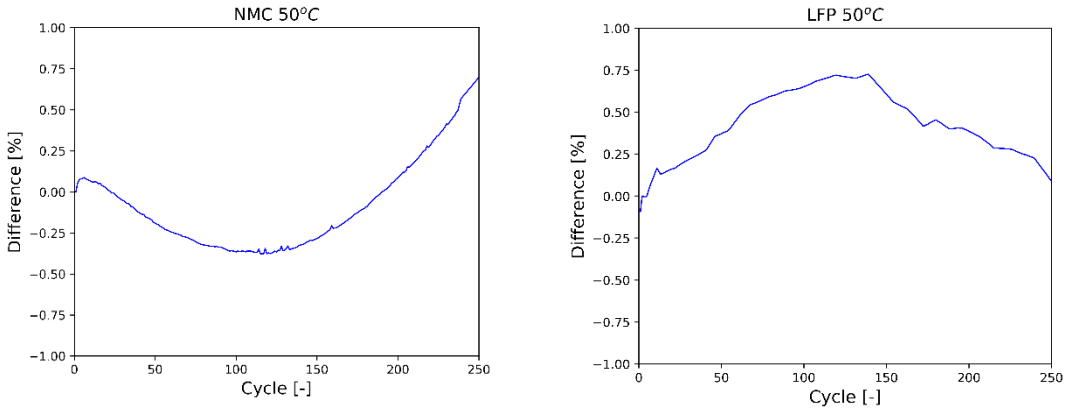

(e) (f)

Figure 20. Calibration of the ageing model by comparing capacity degradation for 250 cycles between numerical model and experimental for NMC absolute values (a), LFP absolute values (b), NMC nomarlized values (c), LFP nomarlized values (d), NMC difference (e) and LFP difference (f) at 50 °C.

Figure 21 (a) and (b) show the model validation for the NMC and LFP cathode chemistries at 20 °C ambient temperature. The model was calibrated, first, with the experimental data obtained at 50 °C ambient temperature, and it was used to predict the battery capacity fade up to 250 cycles at 20 °C. The model reproduced the capacity fade along the cycling process well so that the difference between the computational model and the experimental results was at a maximum of 2% for the NMC battery, as depicted in Figure 21 (c) and (d). It is worth noting that the main mechanisms of lithium losses are triggered at a high temperature, as explained in Figure 11. For this reason, less capacity fade occurred for the condition at 20 °C. The higher error related to the NMC battery, compared to the LFP battery, can be the better understood considering the work developed by Guo et al. [37]. During the first cycles, the graphite structure's enlargement is possibly observed, increasing the Lithium-ion diffusion. However, the model predicted a decrease in capacity fade as an effect of ageing, with a difference of less than 2% for both cathode chemistries.

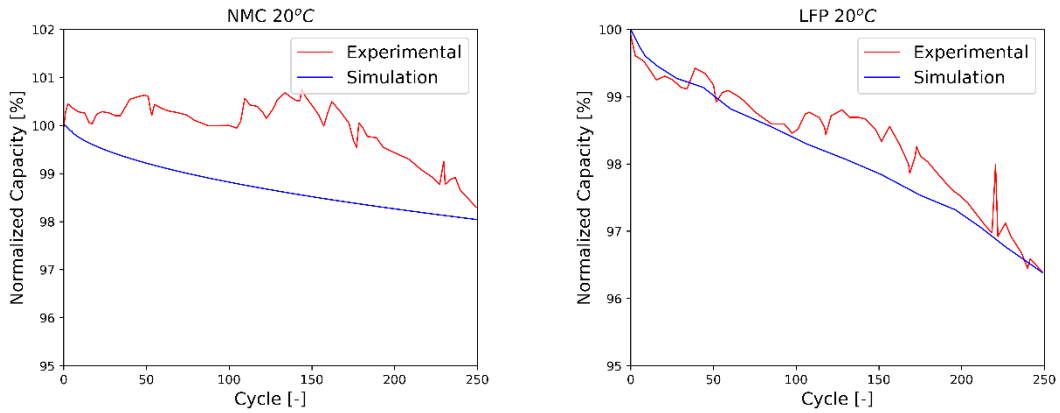

(a) (b)

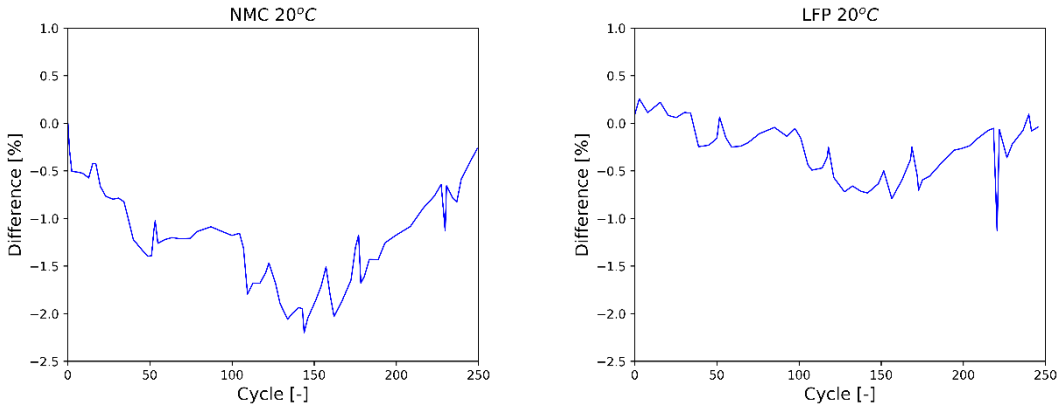

(c) (d)

Figure 21. Validation of the ageing model by comparing capacity degradation for 250 cycles between numerical model and experimental for NMC nomarlized values (a), LFP nomarlized values (b), NMC difference (c), LFP difference (d) at 20 °C.

Figure 22 depicts the capacity fade up to 2000 cycles for the NMC and LFP at 50°C. The advantage of the numerical model is that it allows obtaining the capacity at 2000 cycles without the requirement of further experimental tests. Therefore, it is also possible to estimate the battery end of life. In summary, the model shows that at 2000 cycles, a 20% degradation is reached for the NMC, which is estimated as a maximum for a vehicle application. On the other hand, the LFP shows higher degradation with almost 30% of battery capacity loss at 2000 cycles.

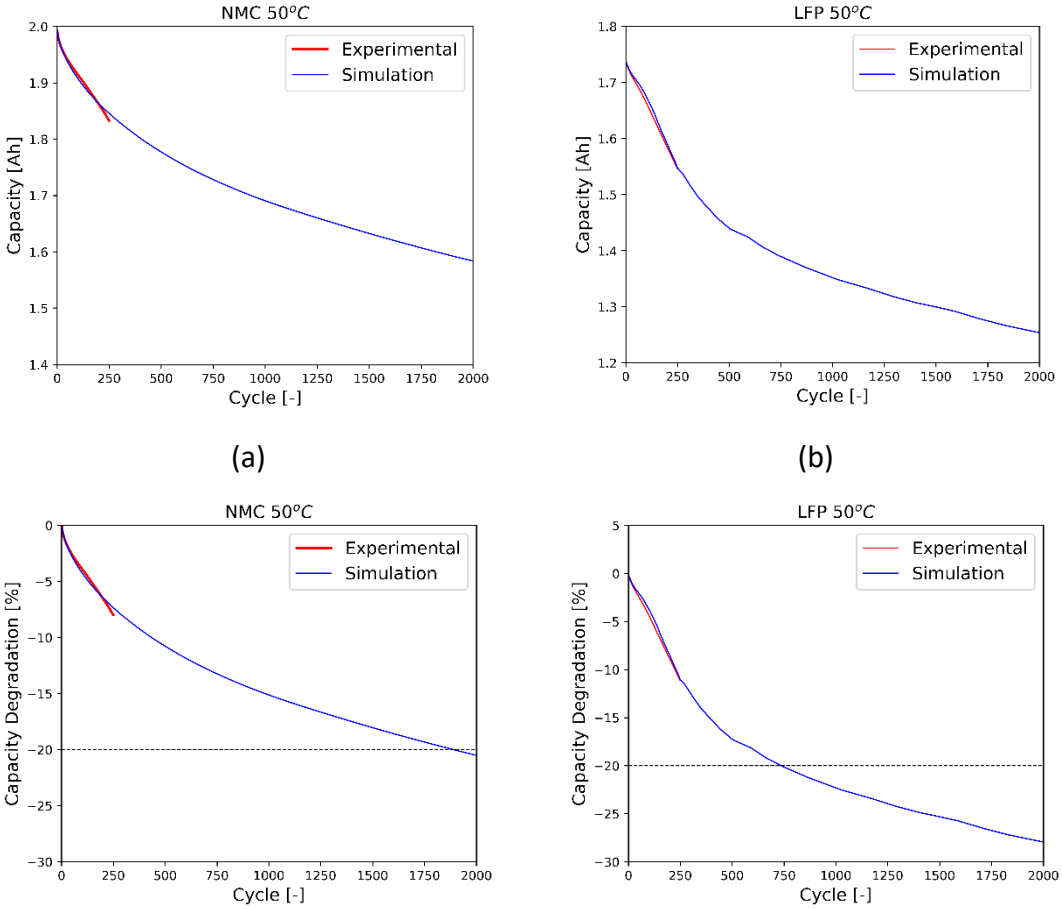

(a) (b)

(c) (d)

(c) (d)

Figure 22. Battery capacity prediction for 2000 cycles compared with the 250 experimental cycles in terms of absolute capacity value for NMC (a), LFP (b) and capacity degradation for NMC (c) and LFP (c) at 50ºC.

The simulation results for the ageing model are used in a complete vehicle model. As mentioned in the methodology, the cells are arranged in parallel and series to achieve 600 V and a total battery energy around 70 kWh. For both packages have the same current, the parallel cells are set as 60 for NMC and LFP. The submodels scheme is depicted in Figure 23. Three driving cycles are simulated representative of homologation conditions (Worldwide Harmonized Light Vehicles Test Cycle Class 3b) and real driving cycles. One represents urban and the second one highway conditions. The routes are collected with GPS in Madrid, Spain. The vehicle weight without battery is 1075 kg, while the frontal area 2.7 m^2, drag coefficient 0.29 and the tire rolling friction factor 0.011 with a tire size of 215/65/R16. The electric machine is modelled with a map-based approach with a maximum power of 150 kW. The driving cycle is run until the battery SOC achieves 20%. The initial SOC is always 100% and the battery temperature 50ºC. The battery electrochemical model is initialized with 1, 500, 1000, 1500, 2000 cycles for represents from a pristine cell to a battery almost in the end of life for a vehicle (capacity below 20% of the initial). The advantage of the simulation is that can be modelled different battery ageing cycles under several driving cycles without expensive experimental tests.

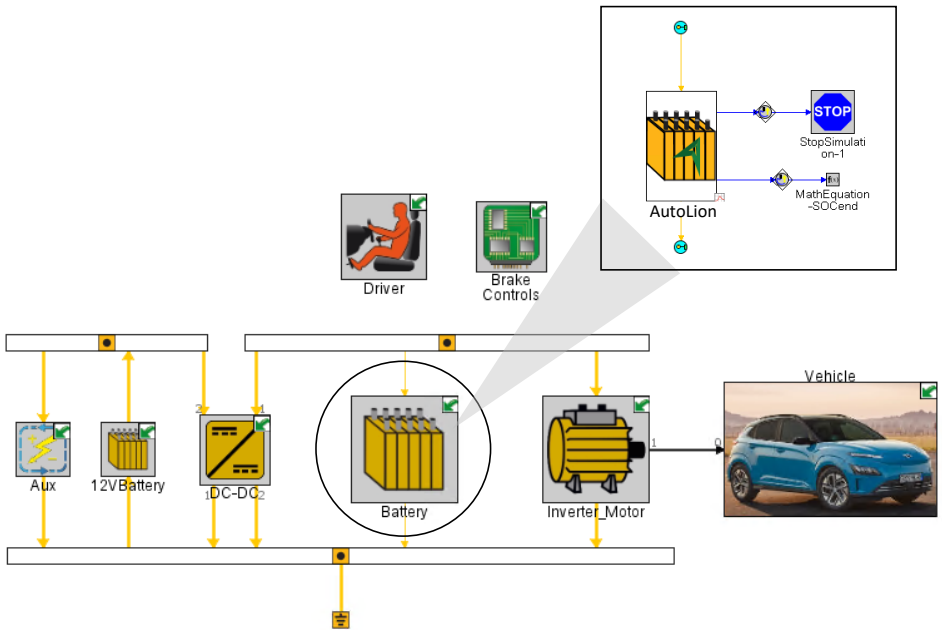

Figure 23. Vehicle model with electrochemical ageing submodel.

The results show, for each cell, in which proportion the driving range is reduced with the ageing cycles (Figure 24). The NMC achieves 390 km when is pristine but loosed 80 km after 2000 cycles. In the case of the LFP, similar reduction suffers the cell (85 km) but the range with pristine condition is 311 km. The difference between cathode chemistries is due to higher battery energy and lower battery weight for the NMC than LFP. The urban cycle results show that EV allows high driving range with above 400 km during the first 250 cycles for the NMC and 330 km for the LFP. The highway is the worst cycle due to high energy consumption due to the vehicle speed and low regenerative

braking. The maximum range in the highway cycle is 245 km for the NMC and 195 km for the LFP under pristine conditions. After 2000 cycles the range decreased to 330 km for the NMC and 140 km for the LFP.

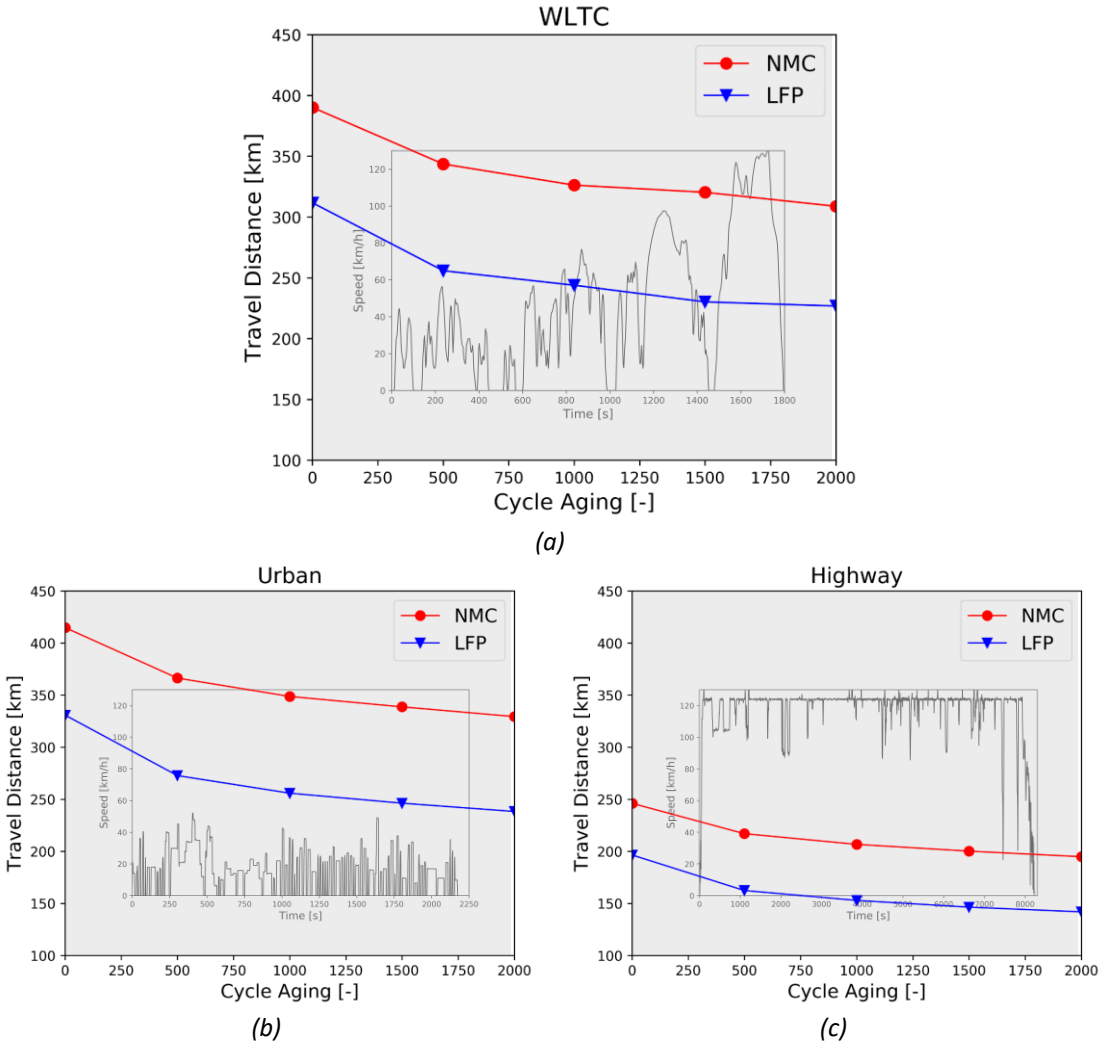

Figure 24. Driving range against cycle ageing for NMC and LFP cathode chemistries in a SUV with 70 kWh. WLTC (a), Urban (b) and Highway (c) conditions are modelled.

4. Conclusions

The present work showed a sequence of experimental tests linked with numeric simulations using GT-Auto-lion. The calibrated and validated model was able to predict performance at cell and battery pack levels. Experimental tests can be summarized as performance tests with different discharge C-rates and driving cycles on pristine NMC and LFP batteries at 20°C and 50°C ambient temperatures. Later, the batteries were aged up to 250 cycles at two different ambient temperatures, 20°C and 50°C, using the same charge, rest and discharge protocol. After that, the performance tests with different C-rates and driving cycles were repeated with the aged batteries. The data obtained were used to calibrate and validate a battery model at different conditions and different current demands (constants and dynamics). As a result, the model delivered a series of geometric aspects related to battery components that can withstand problems related to temperature, capacity loss and serve as a basis for battery modeling. Furthermore, the single cell model was extended to a battery pack model, and a vehicle

level simulation was carried out. The model created for vehicle simulation can predict the ageing effect on battery pack capacity fade under different power demands and conditions, accounting for the decrease in autonomy over the useful life. The vehicle simulation was executed under different driving cycles such as WLTC, urban and highway cycles.

Based on the results, the following conclusions can be drawn:

- An electrochemical model was used to calibrate NMC and LFP cathode chemistry cells. Additionally, the ageing behavior was defined and modeled. Compared to the experimental data, the results indicated good agreement with a difference of less than 2%.
- For both ambient temperatures, the LFP battery degraded more than the NMC battery, resulting in a shorter driving range.
- High ambient temperature sped up the deterioration process during cycling. The validated model has estimated 30% less capacity for the LFP than the NMC battery.
- The discharge voltage curve for the LFP battery was flat as a function of the capacity delivered. Because of this, the LFP battery maintains a steady voltage throughout the driving cycles, enabling an electric car to produce more power.
- As increased the battery capacity delivered, NMC batteries output voltage gradually declined, providing less power for the same current requirement.
- When employed in urban cycles, the vehicle simulation demonstrated better autonomy.
- NMC battery provides 84 km of additional city driving range and 50 km of highway driving range over a LFP battery.
- NMC battery offers 53 km more driving range on the interstate and 91 km more in urban driving at the end of its useful life (20% capacity loss).

The future steps in this work is to increase the number of experimental cycles to be able to calibrate the ageing model by considering not only SEI growth but also lithium plating phenomena. In addition, battery thermal runaway is a hot topic for aged batteries due to the degradation phenomena that increase the probability of cell failure. Therefore, thermal runaway tests in mechanical, electrical and thermal abuse will be conducted with pristine and aged cells.

Acknowledgments

Operación financiada por la Unión Europea a través del Programa Operativo del Fondo Europeo de Desarrollo Regional (FEDER) de la Comunitat Valenciana 2014-2020 con el objetivo de promover el desarrollo tecnológico, la innovación y una investigación de calidad. Proyecto IDIFEDER/2021/53, Equipamiento Para El Estudio Del Fenómeno De Combustión No Controlada En Baterías De Vehículos Eléctricos, entidad beneficiaria Universitat Politècnica de València. The authors also acknowledge Agencia Valenciana de la Innovación for partially supporting this research through DETEBAT-VE project (INNEST/2021/120). This research is part of the project TED2021-130488A-I00, funded by the MCIN/AEI/10.13039/501100011033 and the European Union "NextGenerationEU"/PRTR.

References

[1] García A, Monsalve-Serrano J, Martínez-Boggio S, Wittek K. Potential of hybrid powertrains in a variable compression ratio downsized turbocharged VVA Spark Ignition engine. Energy 2020;195:117039. https://doi.org/10.1016/j.energy.2020.117039.

[2] Katrašnik T, Mele I, Zelič K. Multi-scale modelling of Lithium-ion batteries: From transport phenomena to the outbreak of thermal runaway. Energy Convers Manag 2021;236. https://doi.org/10.1016/j.enconman.2021.114036.

[3] Bais AR, Subhedhar DG, Joshi NC, Panchal S. Numerical investigation on thermal management system for lithium ion battery using phase change material. Mater Today Proc 2022;66:1726–33. https://doi.org/10.1016/j.matpr.2022.05.269.

[4] Newman, John; Balsara NP. ELECTROCHEMICAL SYSTEMS. vol. 1. 4ª. Hoboken, USA: John Wiley & Sons, Inc.; 2021.

[5] Barzacchi L, Lagnoni M, Rienzo R Di, Bertei A, Baronti F. Enabling early detection of lithium-ion battery degradation by linking electrochemical properties to equivalent circuit model parameters. J Energy Storage 2022;50:104213. https://doi.org/10.1016/j.est.2022.104213.

[6] Peled E, Menkin S. Review—SEI: Past, Present and Future. J Electrochem Soc 2017;164:A1703–19. https://doi.org/10.1149/2.1441707jes.

[7] Wang P, Yan D, Wang C, Ding H, Dong H, Wang J, et al. Study of the formation and evolution of solid electrolyte interface via in-situ electrochemical impedance spectroscopy. Appl Surf Sci 2022;596:153572. https://doi.org/10.1016/j.apsusc.2022.153572.

[8] Han X, Lu L, Zheng Y, Feng X, Li Z, Li J, et al. A review on the key issues of the lithium ion battery degradation among the whole life cycle. ETransportation 2019;1:100005. https://doi.org/10.1016/j.etran.2019.100005.

[9] Liao C. Electrolytes and additives for batteries Part I: fundamentals and insights on cathode degradation mechanisms. ETransportation 2020;5:100068. https://doi.org/10.1016/j.etran.2020.100068.

[10] Rechkemmer SK, Zang X, Zhang W, Sawodny O. Empirical Li-ion aging model derived from single particle model. J Energy Storage 2019;21:773–86. https://doi.org/10.1016/j.est.2019.01.005.

[11] Tang X, Wang Y, Zou C, Yao K, Xia Y, Gao F. A novel framework for Lithium-ion battery modeling considering uncertainties of temperature and aging. Energy Convers Manag 2019;180:162–70. https://doi.org/10.1016/j.enconman.2018.10.082.

[12] Löbberding H, Wessel S, Offermanns C, Kehrer M, Rother J, Heimes H, et al. From Cell to Battery System in BEVs: Analysis of System Packing Efficiency and Cell Types. World Electr Veh J 2020;11:77. https://doi.org/10.3390/wevj11040077.

[13] Salvadori A, Grazioli D, Geers MGD. Governing equations for a two-scale analysis of Li-ion battery cells. Int J Solids Struct 2015;59:90–109. https://doi.org/10.1016/j.ijsolstr.2015.01.014.

[14] Vazquez-Arenas J, Gimenez LE, Fowler M, Han T, Chen SK. A rapid estimation and sensitivity analysis of parameters describing the behavior of commercial Li-ion batteries including thermal analysis. Energy Convers Manag 2014;87:472–82. https://doi.org/10.1016/j.enconman.2014.06.076.

[15] Rahn CD, Wang C. Battery Systems Engineering. Wiley; 2013. https://doi.org/10.1002/9781118517048.

[16] Tjaden B, Cooper SJ, Brett DJ, Kramer D, Shearing PR. On the origin and application of the Bruggeman correlation for analysing transport phenomena in electrochemical systems. Curr Opin Chem Eng 2016;12:44–51. https://doi.org/10.1016/j.coche.2016.02.006.

[17] Chung DW, Ebner M, Ely DR, Wood V, Edwin García R. Validity of the Bruggeman relation for porous electrodes. Model Simul Mater Sci Eng 2013;21. https://doi.org/10.1088/0965-0393/21/7/074009.

[18] Vadakkepatt A, Trembacki B, Mathur SR, Murthy JY. Bruggeman's Exponents for Effective Thermal Conductivity of Lithium-Ion Battery Electrodes. J Electrochem Soc 2016;163:A119–30. https://doi.org/10.1149/2.0151602jes.

[19] Smith KA, Rahn CD, Wang CY. Control oriented 1D electrochemical model of lithium ion battery. Energy Convers Manag 2007;48:2565–78. https://doi.org/10.1016/j.enconman.2007.03.015.

[20] Feng X, Ouyang M, Liu X, Lu L, Xia Y, He X. Thermal runaway mechanism of lithium ion battery for electric vehicles: A review. Energy Storage Mater 2018;10:246–67. https://doi.org/10.1016/j.ensm.2017.05.013.

[21] Dickinson EJF, Wain AJ. The Butler-Volmer equation in electrochemical theory: Origins, value, and practical application. J Electroanal Chem 2020;872:114145. https://doi.org/10.1016/j.jelechem.2020.114145.

[22] Hess A, Roode-Gutzmer Q, Heubner C, Schneider M, Michaelis A, Bobeth M, et al. Determination of state of charge-dependent asymmetric Butler-Volmer kinetics for LixCoO2 electrode using GITT measurements. J Power Sources 2015;299:156–61. https://doi.org/10.1016/j.jpowsour.2015.07.080.

[23] Guidelli R, Compton RG, Feliu JM, Gileadi E, Lipkowski J, Schmickler W, et al. Defining the transfer coefficient in electrochemistry: An assessment (IUPAC Technical Report). Pure Appl Chem 2014;86:245–58. https://doi.org/10.1515/pac-2014-5026.

[24] Gozdur R, Guzowski B, Dimitrova Z, Noury A, Mitukiewicz G, Batory D. An energy balance evaluation in lithium-ion battery module under high temperature operation. Energy Convers Manag 2021;227:113565. https://doi.org/10.1016/j.enconman.2020.113565.

[25] Jindal P, Katiyar R, Bhattacharya J. Evaluation of accuracy for Bernardi equation in estimating heat generation rate for continuous and pulse-discharge protocols in LFP and NMC based Li-ion batteries. Appl Therm Eng 2022;201:117794. https://doi.org/10.1016/j.applthermaleng.2021.117794.

[26] Bizeray AM, Zhao S, Duncan SR, Howey DA. Lithium-ion battery thermal-electrochemical model-based state estimation using orthogonal collocation and a modified extended Kalman filter. J Power Sources 2015;296:400–12. https://doi.org/10.1016/j.jpowsour.2015.07.019.

[27] Astaneh M, Andric J, Löfdahl L, Maggiolo D, Stopp P, Moghaddam M, et al. Calibration optimization methodology for lithium-ion battery pack model for electric vehicles in mining applications. Energies 2020;13. https://doi.org/10.3390/en13143532.

[28] SAMSUNG SDI. Material Safety Data Sheet - INR18650-20R. Yongin-Si, Korea: 2013.

[29] Ding MS, Xu K, Zhang SS, Amine K, Henriksen GL, Jow TR. Change of Conductivity with Salt Content, Solvent Composition, and Temperature for Electrolytes of LiPF[sub 6] in Ethylene Carbonate-Ethyl Methyl Carbonate. J Electrochem Soc 2001;148:A1196. https://doi.org/10.1149/1.1403730.

[30] Ma S, Jiang M, Tao P, Song C, Wu J, Wang J, et al. Temperature effect and thermal impact in lithium-ion batteries: A review. Prog Nat Sci Mater Int 2018;28:653–66. https://doi.org/10.1016/j.pnsc.2018.11.002.

[31] Zhang G, Cao L, Ge S, Wang C-Y, Shaffer CE, Rahn CD. In Situ Measurement of Radial Temperature Distributions in Cylindrical Li-Ion Cells. J Electrochem Soc 2014;161:A1499–507. https://doi.org/10.1149/2.0051410jes.

[32] Xu B, Diao W, Wen G, Choe SY, Kim J, Pecht M. Decoupling the thermal and non-thermal effects of discharge C-rate on the capacity fade of lithium-ion batteries. J Power Sources 2021;510:230390. https://doi.org/10.1016/j.jpowsour.2021.230390.

[33] Ning G, Haran B, Popov BN. Capacity fade study of lithium-ion batteries cycled at high discharge rates. J Power Sources 2003;117:160–9. https://doi.org/10.1016/S0378-7753(03)00029-6.

[34] Sun S, Guan T, Shen B, Leng K, Gao Y, Cheng X, et al. Changes of Degradation Mechanisms of LiFePO4/Graphite Batteries Cycled at Different Ambient Temperatures. Electrochim Acta 2017;237:248–58. https://doi.org/10.1016/j.electacta.2017.03.158.

[35] Birkl CR, Roberts MR, McTurk E, Bruce PG, Howey DA. Degradation diagnostics for lithium ion cells. J Power Sources 2017;341:373–86. https://doi.org/10.1016/j.jpowsour.2016.12.011.

[36] Wang L, Qiu J, Wang X, Chen L, Cao G, Wang J, et al. Insights for understanding multiscale degradation of LiFePO4 cathodes. EScience 2022;2:125–37. https://doi.org/10.1016/j.esci.2022.03.006.

[37] Guo J, Li Y, Meng J, Pedersen K, Gurevich L, Stroe DI. Understanding the mechanism of capacity increase during early cycling of commercial NMC/graphite lithium-ion batteries. J Energy Chem 2022;74:34–44. https://doi.org/10.1016/j.jechem.2022.07.005.

Acronyms

ARC	Accelerating rate calorimeter
CCCV	Constant current constant voltage
DoD	Depth of Discharge
ECM	Equivalent circuit model
EV	Electric vehicle
GA	Genetic algorithm
HEV	Hybrid electric vehicle
INR	Lithium-Ion Nickel Rechargeable
LAM	Loss of active material
LCO	Lithium Cobalt Oxygen
LFP	Lithium Ferrum Phosphate
LIB	Lithium ion battery
LLI	Loss of lithium inventory
NMC	Nickel Manganese Cobalt
ODE	Ordinary differential equation
SEI	Solid electrolyte interface
SOC	State of charge
TR	Thermal runaway
DFN	Doyle-Fuller-Newman
WLTC	Worldwide Harmonised Light Vehicles Test Procedure

Nomenclatures

CO_2	Carbon dioxide
E_a	Activation energy
LBT	Arbin's laboratory battery testing
Li	Lithium
Li+	Lithium-ion
F	Faraday's constant
D	Diffusion coefficient
j	Reaction current
A	Transport property
c	Molar concentration of lithium ions
p	Bruggeman tortuosity exponent
r	Radius of the particle
C	Capacitance
k	Ionic conductivity
R	Gas constant/ Resistive film layer/Resistance
T	Temperature
a	Reaction surface area
U	Open-circuit potential of the solid/ Equilibrium potential

q	Specific capacity
$\dot{q}$	Heat flow
f	Normalization terms of error
w	Weight factor
i	Exchange current
n	Bruggeman exponent
M	Molar mass
K	Conductivity of the electrolyte through the porous SEI layer

Subscript

e	Electrolyte
s	Solid phase/ abbreviation in the plural/ specific/ surface
D	Diffusional
u	Universal
SEI	Solid electrolyte interface
c	Cathode/ Contact resistance at the current collectors
a	Anode
max	Maximum
fcc	First charge capacity
fdc	First discharge capacity
th	Theoretical
amb	Ambient
rxn	Redox reactions
rev	Reversable
ohm	Ohmic
V	Voltage
T	Temperature
EC	Electrolyte components
ref	Reference

Superscript

eff	Effective
Li	Lithium
cat	Cathode

Greek symbols

ε	Porosity
σ	Conductivity
ϕ	Potential
α	Charge transfer coefficient
η	Overpotential
γ	Ratio of first discharge and first charge capacity
δ	Thickness
ρ	Density